Materials Advances

REVIEW

View Article Online
View Journal | View Issue

Cite this: *Mater. Adv.*, 2022, 3, 5672

Nanostructured molybdenum dichalcogenides: a review

Priyanka Phalswal, [a] Pawan K. Khanna, *[a] Horst-Günter Rubahn[b] and Yogendra Kumar Mishra [b]

Received 9th February 2022,
Accepted 25th May 2022

DOI: 10.1039/d2ma00150k

rsc.li/materials-advances

With increasing interest in transition metal dichalcogenides (TMDs), a great amount of literature has come into existence covering a broad range of preparation methods as well as their applications in diverse fields. Often dichalcogenides include sulphides, selenides and tellurides; however, they differ in various ways depending upon their crystal structures, methods of synthesis and application requirements. But each TMD is exceptional from the modern technological viewpoint. This review article focuses in detail on the synthesis, properties and applications of molybdenum dichalcogenides [MoX_2 (X = S, Se, Te)] because of the desired expectations of the scientific community for specific types of chalcogenides. The majority of researchers have focused their research on nanocrystalline molybdenum disulphide; however, the present article also discusses selenides and tellurides as they also attract significant interest due to vast new avenues in advanced applications. Through this comprehensive review, we aim to provide a complete description of molybdenum dichalcogenides in one place which will serve as an important source of information for the large number of researchers in the field.

Introduction

Dichalcogenides of transition metals popularly termed as TMDs have captured significant attention due to their layered structure like graphene, accompanied by semiconducting properties. These layered materials are thermally robust, have high dielectric constants and show decent photocatalytic activity owing to a wide variety of chemical structures and compositions. TMDs are a class of compounds consisting of transition metals and chalcogens (S, Se, Te).[1–4] The prominent members of this family are molybdenum dichalcogenides (MoX_2, X = S, Se, Te). Molybdenum is naturally abundant and is the smallest atom of the transition metals to form layered dichalcogenides. These materials offer bandgap tunability and have significant electron mobility in the planes. There is a general understanding that, because of discrete energy level formation, the quantum confinement effect is observed in nanometer-sized semiconducting materials; therefore, they display improved and unique optical, electrical, and structural properties when compared with their bulk counterparts. For example, nano-sized MoS_2 is reported to show enhanced performance as a solid lubricant in comparison to micrometer-sized MoS_2. Therefore, extensive efforts have been made by researchers globally to synthesise MoX_2 in the nanometer regime. Depending upon the synthesis methods, these materials have been obtained in various dimensions (D) and with different morphologies like 0D (nanoplatelets), 1D (nanorods and nanowires), 2D (nanosheets and nanoribbons), and 3D (flowers and snowflakes). The most studied form among these is the 2D form owing to its similarity to graphene. A monolayer of graphene is only one atom thick, while the MoX_2 monolayer consists of molybdenum sandwiched between the layers of chalcogen atoms. The common synthesis methods include exfoliation, chemical vapour deposition, hydrothermal and solvothermal approaches. Because of their multi-dimensional structural properties, MoX_2 have applications in advanced technologies such as in hydrogen evolution reactions,[5–7] light-emitting diodes,[8] solar cells,[9] Li/Na-ion batteries,[10] supercapacitors,[11] field-effect transistors,[12,13] photo-detectors,[14] bio-sensors,[15–17] solid lubricants, dehydrosulfurization,[10] photocatalysis,[18] desalination of water[19,20] and the biomedical field.[21] Therefore, studying these materials allows us to go beyond graphene and explore new properties of 2D inorganic materials. The current review discusses the exciting properties of MoX_2 with a focus on their synthesis and application in energy devices.

Crystal phases and molecular structures

MoX_2 compounds are composed of vertically stacked hexagonal layers of Mo covalently bonded to hexagonal layers of X atoms and these layers are held together by weak van der Waals forces.

[a] *Nano Chemistry and Quantum Dots R & D Laboratory, Department of Applied Chemistry, Defence Institute of Advanced Technology (DIAT), Ministry of Defence, Govt. of India, Girinagar, Pune-411025, India.*
E-mail: pawankhanna2002@yahoo.co.in
[b] *NanoSYD, Mads Clausen Institute, University of Southern Denmark, Alsion 2, 6400, Sønderborg, Denmark*

They are highly anisotropic, and it is reported that the conductivity values are around 100 times lower in the perpendicular direction than those in the MoS_2 planes. A similar trend is observed for electrical properties. These materials exist in various polymorphic forms, mainly 2H and 1T. The trigonal prismatic coordination is observed in the 2H phase showing

Priyanka Phalswal

Priyanka Phalswal obtained her BSc degree from Maharshi Dayanand University, Rohtak, Haryana, in the year 2015. During her BSc, she received the "Promotion of Science and Education (POSE)" scholarship from the Department of Science & Technology (DST), Govt. of Haryana, India. Continuing her studies, she received an MSc degree in Applied Chemistry from Malviya National Institute of Technology, Jaipur, India, in 2017. She is currently pursuing her PhD under the able guidance of Prof. P. K. Khanna at the Defence Institute of Advanced Technology, Pune, India. She has published 7 research papers in reputed international journals. She is a life member of the "Society for Materials and Chemistry (SMC)", BARC, Mumbai. Her research interests include nanomaterials, quantum dots, materials chemistry and their energy applications.

Pawan K. Khanna

Dr Pawan Kumar Khanna received his PhD in organo-metallic chemistry of Se & Te from the Indian Institute of Technology, Bombay in 1989–1990. He did his post-doc at the Queens University of Belfast and the University of Wales at Swansea (UK) in the group of Prof. Christopher P Morley during 1989–1992. Later on, he joined C-MET, Pune. He was awarded the BOYSCAST fellowship of DST, Govt of India, during 1998–1999 to work on quantum dots driven at the University of St. Andrews, Scotland (UK), with Professor David J Cole-Hamilton. He is currently a Professor in the Dept. of Applied Chemistry at the Defence Institute of Advanced Technology, Pune, India. His research interests include nanochemistry and nanomaterials, e.g. quantum dots, nano-inks, and nano-fluids, for energy and biological applications. He has published over 200 research papers. He has recently been named as a top 1% materials scientists in the world by a study conducted by the researchers of Stanford University, USAm published by Elsevier. He has guided more than 60 master, doctoral and post-doctoral researchers and completed 20 research projects funded by government agencies.

Horst-Günter Rubahn

Horst-Günter Rubahn is a professor and director of the Mads Clausen Institute at the University of Southern Denmark. He also leads the nanotechnology center NanoSYD. Besides a doctoral title and a habilitation from the University of Göttingen he owns an honorary doctoral title from Kaunas University of Technology. He is appointed Danish national expert nanotechnology in the Horizon 2020 Programme Committee NMBP and chair of the international PhD school PCAM. Horst-Günter Rubahn's recent research focuses on the development of generic routes towards novel thin film smart materials and nanomaterials. This includes the complete range from fundamental via applied research to device integration.

Yogendra K. Mishra

Yogendra Kumar Mishra is Professor MSO and leader of the Smart Materials group at Mads Clausen Institute, NanoSYD, University of Southern Denmark (SDU). Prior to SDU, he was leading a group at Functional Nanomaterials Chair, Kiel University, Germany in continuation with an Alexander von Humboldt fellowship. He did habilitation (2015) in Materials Science at Kiel University and PhD in Physics (2008) at Jawaharlal Nehru University (JNU) New Delhi, India. He developed a new flame-based process for tetrapod nanostructuring and their 3D networks as cellular solids which found many applications including their use as sacrificial templates for new materials structuring. The Smart Materials group's main focus is to develop a new class of advanced materials for future green and sustainable technologies.

semiconducting properties, while in 1T the central atom is octahedrally coordinated, and it is metallic in nature. In a trigonal prismatic structure, the atoms' packing is AbA type, while in an octahedral structure it is AbC type (capital letters denote chalcogen atoms and the lowercase letter denotes a metal atom).[22] The 1T phase shows better activity in hydrogen evolution and energy storage than the 2H phase.[23]

The Earth's crust contains MoS_2 in the form of molybdenite. It exists in three polymorphic phases – 1T, 2H, and 3R belonging to point groups D_{6d}, D_{6h} and C_{3v}, respectively. Here, the numerals 1, 2 and 3 indicate the numbers of layers and T, H, and R denote tetragonal, hexagonal, and rhombohedral structures, respectively. The crystal structure for all the three phases is depicted in Fig. 1.[24] Naturally, MoS_2 occurs in the 2H phase. Mo coordinates octahedrally in the 1T phase and exhibits paramagnetic behaviour. It transforms into a more stable form, *i.e.*, 2H-MoS_2, upon aging or heating *e.g.* when Guo *et al.*[25] annealed 1T′-MoS_2 to 300 °C in an Ar atmosphere, it transformed to 2H-MoS_2 with stability up to ~1200 °C, thereafter it is converted to Mo_2S_3. 3R-MoS_2 has Mo in trigonal prismatic coordination and transforms to its 2H-prototype upon heating.[10] Guo *et al.*[25] reported a phase change by intercalation with alkali metal ions. This transformation is attributed to the change in the electronic structure from d^2 to d^3, which leads to destabilisation in the trigonal prismatic 2H phase and conversion to the octahedral 1T phase. The S–Mo–S layer-to-layer distance is about 6 Å.

Similarly, $MoSe_2$ is also found in the Earth's crust as a scarce mineral drysdallite. 2H-$MoSe_2$ with the hP_6 space group has cell parameters of a = 3.283 Å and c = 12.918 Å. The electron mobility is higher in 2D $MoSe_2$ than that in 2D MoS_2. Bond lengths of 2.528 Å for Mo–Se and about 3.293 Å for Se–Se make them better candidates for various applications. $MoSe_2$ monolayers are thicker than MoS_2 because of the large atomic radius of Se atoms.[26] Fig. 2 represents the crystal structure of $MoSe_2$ which is analogous to that of MoS_2.[27]

$MoTe_2$ crystallises in two phases, *i.e.*, 2H and 1T′, whose crystal structure is presented in Fig. 3.[28] The 2H phase belongs

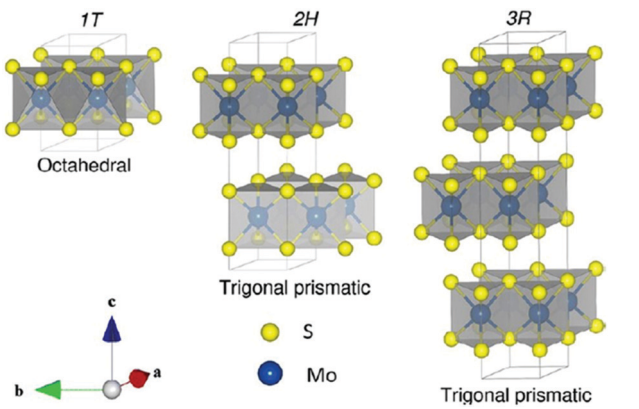

Fig. 1 Unit cell structure of various polymorphs of MoS_2. Reprinted with permission from ref. 24 [A. Kuc, in *Chemical Modelling: Volume 11*, The Royal Society of Chemistry, 2015, vol. 11, pp. 1–29]. Copyright The Royal Society of Chemistry.

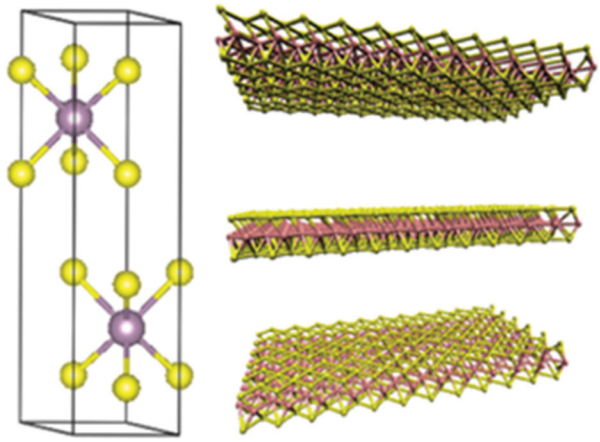

Fig. 2 Crystal structure of 2H-$MoSe_2$ Reprinted with permission from ref. 27 [S. Tongay, J. Zhou, C. Ataca, K. Lo, T. S. Matthews, J. Li, J. C. Grossman and J. Wu, *Nano Lett.*, 2012, **12**, 5576–5580]. Copyright 2012 American Chemical Society.

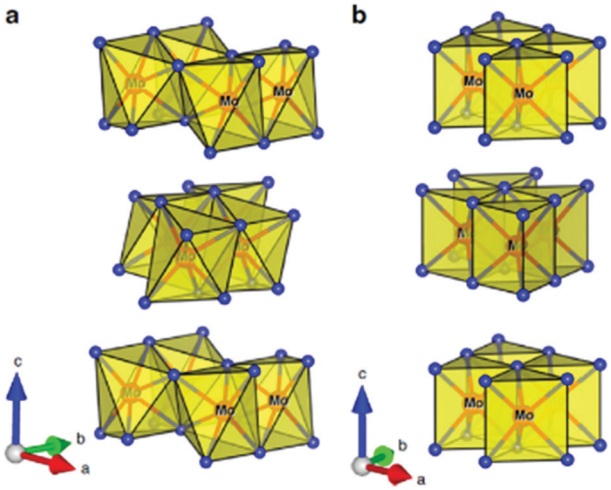

Fig. 3 Crystal structure of (a) monoclinic 1T′-$MoTe_2$ and (b) hexagonal 2H-$MoTe_2$ phases. Reprinted with permission from ref. 28 [J. C. McGlynn, T. Dankwort, L. Kienle, N. A. G. Bandeira, J. P. Fraser, E. K. Gibson, I. Cascallana-Matias, K. Kamaras, M. D. Symes, H. N. Miras and A. Y. Ganin, *Nat. Commun.*, 2019, **10**, 4916]. Copyright 2019, The Authors.

to the *hP*6, $P6_3/mmc$ space group with unit cell sizes of a = 3.519 Å and c = 13.946 Å. The 1T phase belongs to the *mP*12, $P2_1/m$ space group with unit cell constants of a = 6.33 Å, b = 3.469 Å, and c = 13.86 Å. The unit cell sizes change with temperature due to thermal expansion as the energy gap between these phases is very low (40 meV).[29] It is reported that the 2H-phase is slightly less stable, *i.e.*, 815 °C and beyond that it changes to the more stable phase of 1T′ which is stable even beyond 900 °C.[30] Due to the weak bonding between Mo and Te, its synthesis in one pure phase is highly challenging, thus limiting its exploration and applications. Therefore, it is desired to conduct research in materials like $MoTe_2$ with rapid pace. The role of chemists therefore becomes more demanding to propose simpler methods for the synthesis of pure phase $MoTe_2$.

Table 1 Comparison of bandgap values at the nano- and bulk level

MoX_2	Bulk bandgap	Bandgap in the nano-regime
MoS_2	Indirect (E_g = 1.2 eV)[33]	Direct (E_g = 1.8 eV)[34]
$MoSe_2$	Indirect (E_g = 1.1 eV)	Direct (E_g = 1.55 eV)[27,35]
$MoTe_2$	Indirect (E_g = 0.93 eV)	Direct (E_g = 1.1 eV)[29]

Electronic properties

On moving from bulk to nano-scale, MoX_2 give rise to diversified properties due to their transformation from indirect to direct bandgap semiconductors. It is well known that upon particle size reduction the bandgap increases in semiconductor materials and MoX_2 are no exception to that. The bandgap values of these materials in bulk and the nano range are summarised in Table 1. The bandgap for bulk MoS_2 is about 1.2 eV which can reach up to 1.8 eV for nano-MoS_2 and thus IR-active MoS_2 can be converted to visible active, which makes it a potential photocatalyst. Similarly, $MoSe_2$ has been reported to attain a bandgap of 1.5 eV in the nano-regime, thus extending its scope in optoelectronic applications. Likewise, bulk 2H-$MoTe_2$ has an indirect bandgap of 0.93 eV, whereas a direct bandgap of 1.1 eV is reported for monolayer 2H-$MoTe_2$.[31] This value is very close to that of Si, and hence it finds numerous applications in photonics. As the bandgap of $MoTe_2$ lies in the infrared region, it can be used as an infrared detector. It is also reported that $MoTe_2$ can exhibit a higher phonon mobility than MoS_2 at room temperature.[32]

The bandgap in MoX_2 decreases gradually from 1.8 to 1.1 eV as the size of the chalcogen increases. Therefore, it also gives an opportunity to tune the bandgap using different concentrations of chalcogens.[36–38] In MoX_2, Mo is in the +4 oxidation state having a $4d^2$ valence electronic configuration. In a trigonal prismatic structure, the electrons are filled in the d_{z^2} orbital and the transition from this orbital to the $d_{x^2-y^2}$ and d_{xy} orbitals makes it semiconducting in nature, while in octahedral coordination, the electrons are filled in the t_{2g} orbital (as unpaired in d_{xy} and d_{yz}) which corresponds to the valence band in the electronic structure of the 1T phase (Fig. 4).[22] This partially occupied valence band in the 1T phase is responsible for its semi-metallic nature.[39] As the d_{z^2} orbital has a slightly lower energy than the t_{2g} orbital, the overall energy of electrons is lower for the 2H phase, making it thermodynamically more stable than the 1T phase. Additionally, the lone pairs of chalcogens terminate the edges of layers, giving them stability against reaction with environmental species.[22]

Synthesis

Several approaches are documented for the synthesis of nano-MoX_2. As the MoX_2 layers are linked together through van der Waals forces, these forces can easily be dealt with to obtain few/monolayers of these materials conveniently from the bulk forms. Some notable approaches for the synthesis of nano-MoX_2 practiced by researchers are hydrothermal, solvothermal, thermal decomposition, ultrasonication, chemical vapour deposition, microwave, mechanical exfoliation and chemical exfoliation.

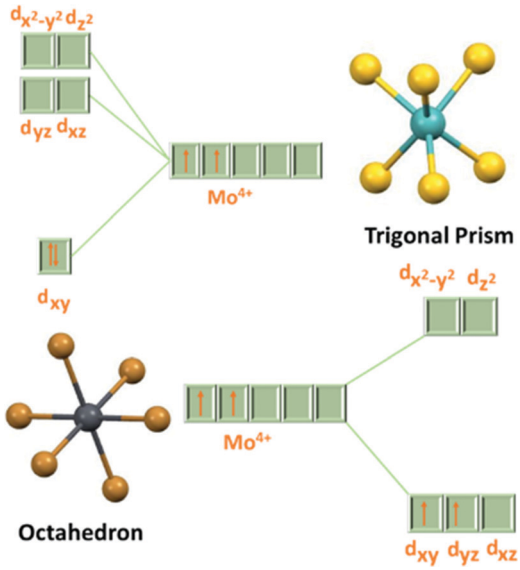

Fig. 4 d-orbital splitting diagram in trigonal prismatic and octahedral coordination.

These techniques result in a wide diversity of morphologies. The commonly used molybdenum precursors are molybdenum trioxide, ammonium heptamolybdate (AHM), and sodium molybdate and the synthesis methods are discussed one by one in the following sub-sections.

Hydrothermal method

The hydrothermal method is a technique used to carry out chemical reactions at high temperatures and pressures. A properly sealed vessel, generally a Teflon lined stainless-steel autoclave, is used. The precursors and chemical reagents are dissolved in water and kept in an autoclave at high temperatures for long durations. Hydrothermal synthesis of molybdenum dichalcogenides has been extensively reported. Li *et al.*[40] successfully synthesized MoS_2 nanowires *via* a hydrothermal method. Prabhakar *et al.*[41] synthesised MoS_2 nanoflowers and nanosheets of less than 100 nm diameter and 10–50 nm thickness by the reaction of AHM with thioacetamide and thiourea, respectively, and using citric acid as a surfactant. The sulphur source was added to a moderately acidic aqueous solution of AHM and citric acid and then kept in an autoclave for about 10 h at 160 °C to collect a black powder. Similarly, by use of an autoclave, Tian *et al.*[42] reported a green protocol for synthesis of MoS_2 fine crystals using Na_2MoO_4 and potassium thiocyanate (KSCN) as precursors sealed in a stainless-steel autoclave at 260 °C for 24 h. They reported silvery dark crystalline nanosheets with a size of 0.3 μm from transmission electron microscopy (TEM) images. The suggested reaction is represented by eqn (1):

$$4MoO_4^{2-} + 9SCN^- + 15H_2O \rightarrow 4MoS_2 + SO_4^{2-} + 3NH_4^+ + 9CO_3^{2-} + 6NH_3 \quad (1)$$

Nagaraju *et al.*[43] prepared bundles of MoS_2 nanofibres *via* two different routes using AHM as the molybdenum precursor

and sodium sulfide or H_2S gas as the source of sulfur in the presence of citric acid as a surfactant. These reaction mixtures were sealed in an autoclave and kept at 180 °C for 48 and 24 h, respectively, depending on the source of sulfur. It is reported that, irrespective of the source of sulfur, the products from both the reactions have similar morphology, with the diameter of nanorods being about 150–300 nm and length being 20–25 μm based on scanning electron microscopy (SEM) images. It was demonstrated that the role of citric acid is very crucial to avoid the formation aggregates and impurities of MoO_3. The reaction in the presence of citric acid is represented by eqn (2) and (3) showing that $(NH_4)_2MoSO_4$ is formed as an intermediate.

$$NH_4MoO_4 + 4Na_2S + C_6H_8O_7 \rightarrow (NH_4)_2MoS_4 + Na_7C_6H_4O_7 + 4NaOH \quad (2)$$

$$(NH_4)_2MoS_4 \rightarrow MoS_2 + N_2 + 2H_2 + 2H_2S \quad (3)$$

Pourabbas *et al.*[44] compared the formation of nano-ribbons of nano-MoS_2 *via* two different methods where, in the first case, MoO_3 was mixed with Na_2S in water and autoclaved for 12 h at 300 °C to isolate large poly-disperse particles with a size in the range of 150–200 nm composed of nanoribbons of 2–3 nm thickness and about 100 nm length. However, a better size domain was obtained when the authors dispersed AHM and thiourea in water with 1-octanol and sodium lauryl sulphate as surfactants, sealed them in an autoclave at 180 °C for 5 h and obtained particles in the size range of 20–30 nm in the form of ribbons with uniform distribution. Synthesis of relatively small particles of 3R-MoS_2 with a mean diameter of about 5.5 nm was reported by Manuja *et al.*[45] by autoclaving the aq. mixture of Na_2MoO_4, polyethylene glycol (PEG) and thiourea at 200 °C for 11 h. Hou *et al.*[46] synthesised spherical and flower-like MoS_2 nanoparticles by modifying the additive used such as CTAC, PEG and ethyl alcohol in the reaction of sodium molybdate and thioacetamide. Sodium molybdate and thioacetamide were taken in the stoichiometric ratio, and then the additive was added with some amount of water. They further acidified the mixture to set the pH to 1 and the mixture was then sealed in an autoclave and heated in a muffle furnace for 6 h at 220 °C. The course of the reaction is represented by eqn (4)–(9). The authors found that spherical nanoparticles were obtained using CTAC and PEG as additives with little difference in their sizes, whereas flower-like MoS_2 NPs were obtained using ethanol.

$$CH_3CSNH_2 + 2H_2O \rightarrow CH_3CONH_4 + H_2S \quad (4)$$

$$Na_2MoO_4 + 4H_2S \rightarrow Na_2MoS_4 + 4H_2O \quad (5)$$

$$Na_2MoS_4 + 4HCl \rightarrow H_2MoS_4 + 2NaCl \quad (6)$$

$$Na_2MoS_4 + H_2SO_4 \rightarrow H_2MoS_4 + Na_2SO_4 \quad (7)$$

$$H_2MoS_4 \rightarrow MoS_3\downarrow + H_2S \quad (8)$$

$$MoS_3 \rightarrow MoS_2\downarrow + S \quad (9)$$

Similarly, there is an extensive use of the hydrothermal method for the synthesis of nanocrystalline $MoSe_2$.[47–51] Common selenium precursors often employed are Se and Na_2SeO_3. Several researchers described excellent use of the hydrothermal method to obtain $MoSe_2$, *e.g.* the mixture of Na_2MoO_4, hydrazine hydrate/L-ascorbic acid and Se in distilled water can be processed in an autoclave for several hours at 200 °C to obtain flower-like morphology made up of very thin nanosheets,[14,52] as supported by high resolution transmission electron microscopy (HRTEM) images (Fig. 5).

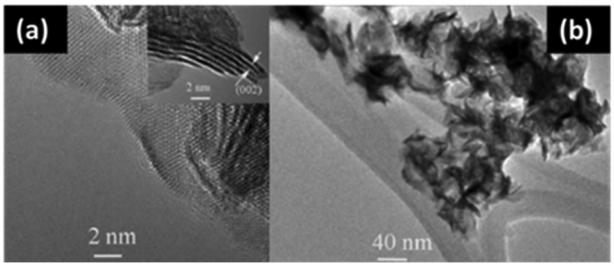

Fig. 5 HRTEM image of $MoSe_2$ prepared by a hydrothermal method. Reprinted with permission from ref. 52 [H. Tang, K. Dou, C.-C. Kaun, Q. Kuang and S. Yang, *J. Mater. Chem. A*, 2014, **2**, 360–364.]. Copyright The Royal Society of Chemistry.

The typical XRD and UV absorption spectra of $MoSe_2$ formed by this method are shown in Fig. 6.[14] The XRD results supported that the 2H phase was formed and the absorption was observed at ~450 nm and ~650 nm, indicating that the thus-formed compound is a useful photo-sensor in the range of 400–700 nm. Modifications and alterations are often performed by different groups to enhance the product yield as well as the properties for making them suitable for a variety of applications. In one such modification, a pH-based synthesis has been explored by Mittal *et al.*[53] to study its impact on the size and morphology of $MoSe_2$. Nanosheets and nano-urchins that contained several nanospheres were obtained at pH 5 and pH 8, respectively, *via* a three-step mechanism. In the first step, hydrazine hydrate reduced selenium to give selenium ions as per eqn (10). When this solution was added to a solution of sodium molybdate in water, excess hydrazine hydrate reduced Mo^{6+} ions in Na_2MoO_4 to Mo^{4+} ions (eqn (11)). Finally, the product was formed as per eqn (12) where the reaction between molybdenum and selenium ions took place in an autoclave.

$$5N_2H_4 + 2Se \rightarrow N_2 + 4N_2H_5^+ + 2Se^{2-} \quad (10)$$

$$2MoO_4^{2-} + N_2H_4 + 4H_2O \rightarrow 2Mo^{4+} + N_2 + 12OH^- \quad (11)$$

$$Mo^{4+} + 2Se^- \rightarrow MoSe_2 \quad (12)$$

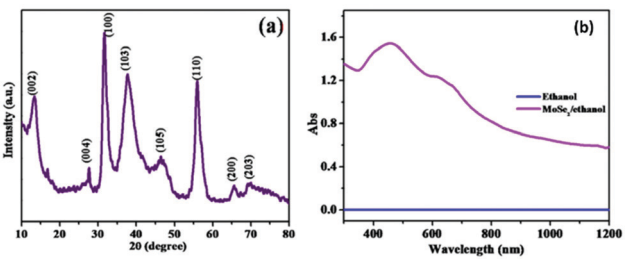

Fig. 6 XRD and UV-Vis spectra of 2H-$MoSe_2$. Reprinted with permission from ref. 10 [N. T. Shelke and D. J. Late, *Sens. Actuators, A*, 2019, **295**, 160–168]. Copyright 2019, Elsevier.

In similar efforts, Xiao *et al.*[54] used sodium molybdate and selenium powder with various amounts of basic reducing agent such as $NaBH_4$ to synthesize $MoSe_2$ in mixed 1T and 2H phases where it has been described that by increasing the amount of $NaBH_4$, the number of stacked layers can be decreased. Likewise, $MoSe_2$ nanorods and spherical particles were synthesized by Ghritlahre *et al.*[55] using a basic aq. solution of sodium molybdate or AHM as the molybdenum precursor and Se powder with a small amount of hydrazine hydrate (HH) in an autoclave at 200 °C.

Often it is realized that the source of selenium is a tricky choice and it is crucial for the preparation of the product of desired morphology and physical properties. Thus, researchers constantly explore a variety of such combinations and look for newer, unexplored and more appropriate selenium precursors to suit the metal precursors for establishing the appropriate kinetics. Inorganic selenium precursors may offer more versatility in surface properties when compared with selenium metal as a source. Setayeshgar *et al.*[56] were the first to use sodium selenite as the selenium source for the synthesis of nanocrystalline $MoSe_2$. This eliminated the requirement of any reducing agent like hydrazine hydrate as Na_2SeO_3 readily dissociates in water to give Se^{2-} ions. They proposed that the reaction of $MoCl_5$/NaOH/ethylene glycol and Na_2SeO_3 can yield bi-phase 1T, 3.5-to-6 nm thick 2H-$MoSe_2$ nanosheets of 5 to 8 layers *via* autoclave heating at 200 °C for 18 h. The fine tuning of the size and morphology was reported by varying the ratio of reagents and precursors. The suggested chemical reactions in this process are represented by eqn (13) and (14).

$$2MoCl_5 + 8NaOH \rightarrow 2Mo(OH)_4 + 8NaCl + Cl_2 \quad (13)$$

$$2Na_2SeO_3 + Mo(OH)_4 + NaCl + H_2O \rightarrow MoSe_2 + 5NaOH + HCl + 3O_2 \quad (14)$$

It is noticed that $MoCl_5$ was reduced to Mo^{4+} in the first stage, followed by *in situ* release of Se^{2-} from Na_2SeO_3. In another study, Liu *et al.*[57] used potassium selenocyanate as the selenium source with AHM in the water/ethylene glycol (EG) mixture and synthesized $MoSe_2$ microspheres consisting of $MoSe_2$ nanosheets. According to them, potassium selenocyanate dissociates to give H_2Se in the reaction as per eqn (15) which reacts with Mo^{4+} ions produced in the mixture to give $MoSe_2$.

$$NCSeCH_2COO^- + H^+ \rightarrow CO_2 + NH_3 + H_2Se \quad (15)$$

With set methodologies for sulphides and selenides, counterpart tellurides have not been much explored but still there are a few reports on its hydrothermal synthesis, *e.g.* Li and co-workers[58] synthesized $MoTe_2$ nanosheets having thickness in the range of 20–80 nm. Te powder was mixed with water in the presence of $NaBH_4$, followed by addition of sodium molybdate with continuous stirring and heating. The mixture was then transferred to an autoclave and maintained at 200 °C for 48 h. Diffraction peaks at 12.66° (002), 25.48° (004), 29.9° (100), 29.99° (101), 35.17° (103), 43.93° (105), 51.94° (110), 52.33° (008) and 64.28° (203) were seen in the XRD spectrum of 2H-$MoTe_2$. Although the method offers easy processing and a green alternative, products of uncertain/mixed morphology are obtained.

Solvothermal method

Solvothermal and hydrothermal methods are analogues, except that the organic solvents are used instead of water for the synthesis. The precursor and solvent mixture are sealed in a vessel and the reaction is carried out at a temperature more than the boiling point of the solvent. The Mo–chalcogenide synthesis reactions require a very high temperature/energy as the precursors like MoO_3 and chalcogen sources often do not break/dissociate easily at normal temperatures. In such a situation solvothermal methods for synthesis of nanomaterials are considered very handy to obtain uniform sized particles. Zhan *et al.*[59] synthesised uniform thin platelets of MoS_2 (100 nm thickness) from MoO_3 and elemental sulphur using hydrazine in pyridine in an autoclave that was maintained at 300 °C for 12 h. They proposed that, firstly, MoO_3 may be reduced to MoO_2 by hydrazine hydrate and, on the addition of sulphur powder, O-atoms are replaced by S-atoms to form MoS_2 nanoparticles (NPs). The reaction methodology is depicted in Fig. 7.

Similarly, Li *et al.*[60] mentioned the synthesis of free MoS_2 in a single step where $(NH_4)_2MoS_4$ and $N_2H_4{\cdot}H_2O$ were mixed in DMF and heated in a Teflon-lined autoclave at 200 °C for 10 h. They, initially, synthesized MoS_2 particles on graphene and elaborated that even without graphene free standing MoS_2 can be prepared from this method. Such an approach was found to be useful for catalytic applications. The formation of a colloidal solution of MoS_2 nanosheets was reported by Zhu *et al.*[61] from micro MoS_2 powder dispersed in *n*-hexane and reacted with *n*-butyllithium (*n*-BuLi) in an autoclave for 5 h at 100 °C. The MoS_2 nanosheets were obtained *via* repetitive washing of the intermediate compound Li_xMoS_2, followed by its hydrolysis by sonication for 1 h in water. Similarly, flower like nanoparticles composed of ultrathin nanosheets of MoS_2 have been reported by use of the sodium molybdate, thiourea and hydroxylamine hydrochloride mixture (1 : 2 : 2 molar ratio) in an autoclave heated for 24 h at 190 °C, followed by annealing for 5 h at

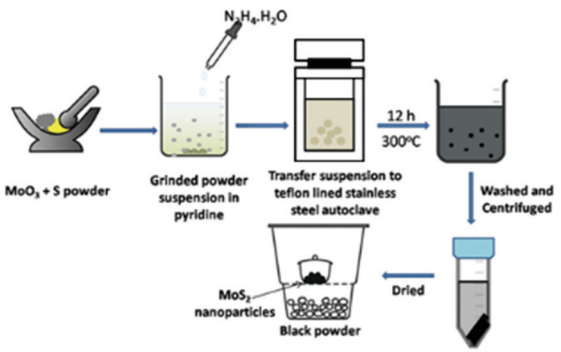

Fig. 7 Preparation of MoS_2 NPs in an autoclave using MoO_3 (ref. 59).

500 °C.[62] The authors observed that a lower temperature and reaction time leads to formation of MoO_2 impurities.

Several researchers have also reported synthesis of nano-$MoSe_2$ by the solvothermal method using an autoclave. The synthesis method is very much similar to that of MoS_2 where only the sulphur source is replaced by a selenium source. The most commonly used precursors are MoO_3 and Se powder with some reducing agents like $N_2H_4{\cdot}H_2O$.[63] Jiang *et al.*[64] suggested that the thickness of $MoSe_2$ nanosheets can be decreased with increasing carbon chains in alcohol when performing the synthesis using various solvents like ethanol, butanol, hexanol and octanol. They also commented on the morphology with respect to the reaction temperature. The particles formed at 120 °C were spherical in shape with no clear evidence of nanosheets. When the temperature was increased, nanoflowers composed of thin nanosheets were observed; with further increase in temperature, these nanosheets became thicker.

Despite the popularity of the solvothermal method, it has limitations for high melting solids which have poor or no solubility. Therefore, compounds like $MoTe_2$ have not been popularly synthesized by this method unlike by the hydrothermal method where synthesis of $MoTe_2$ nanosheets has been possible with ease *via in situ* reduction of Te powder by $NaBH_4$ which is useful in generating Te^{2-} ions. Similarly, the reaction medium in the solvothermal method may have its utility for $MoTe_2$ formation. It is challenging, however, to monitor the pressure during the synthesis and the nature of solvents *versus* the duration/pressure may limit its operational understanding.

Thermal method

The generally adopted methods are mostly based on the autoclave requirement which requires special skills to operate and, hence, is highly challenging. It is always desirable that simpler methods be developed for enhancement of the applicability of materials with ease. In this regard, direct reactions in standard laboratory glassware are generally favourable and preferred. The thermal method, therefore, being the most conventional, brings its own advantages. By this method, researchers can monitor the reaction changes physically as well as spectroscopically at desired time intervals during the course of reactions. The precursors in such methods are solvent-friendly in terms of dispersion/solubility. Some of the popular reagents are metal complexes, molecular precursors and/or chalcogen sources which react at normal pressure and at a temperature below 300 °C. There are a number of reports where soft solution methods have been practiced. For example, Duphil *et al.*[65] synthesised MoS_2 by thermal decomposition of $Mo(CO)_6$. The sulphur powder was dissolved in *p*-xylene by heating, followed by the addition of $Mo(CO)_6$ at room temperature and refluxing at 140 °C for several hours. The reaction setup is shown in Fig. 8. Raman spectroscopy was extensively and effectively applied for monitoring the reaction by way of disappearance of the CO peak as the formation of a black precipitate starts. It was opined that $Mo(CO)_6$ decomposed to give elemental Mo, followed by its reaction with the S present to give a black precipitate of MoS_2 of 10–30 nm size albeit not

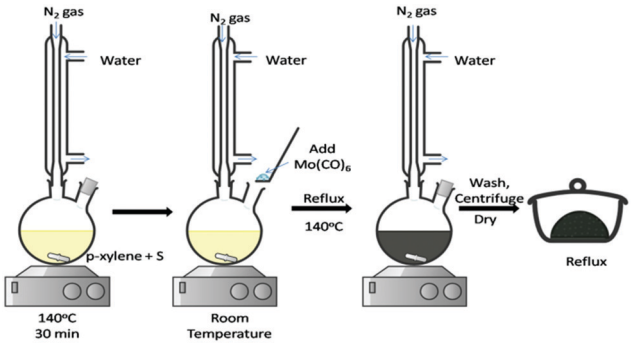

Fig. 8 Reaction between $Mo(CO)_6$ and S under a nitrogen atmosphere to synthesise MoS_2 NPs.[65]

without aggregation. The overall reaction is represented by eqn (16):

$$Mo(CO)_6 + 2S \rightarrow MoS_2 + 6CO \quad (16)$$

Park *et al.*[66] reported preparation of MoS_2 *via* generation of a colloidal solution of Mo NPs, followed by its reaction with sulphur *via* a thermal method. In this method, $Mo(CO)_6$ and S were reacted in the presence of oleic acid to control the particle size. The reaction consists of two steps – (1) formation of polycrystalline Mo/MoO_x nanoflakes and (2) reaction with sulphur to produce MoS_2. By this method, highly crystalline and spherical MoS_2 NPs of about ~2 nm size were obtained. The schematic illustration is shown in Fig. 9.

It is well documented and understood by this time that chemical methods can produce high quality nanostructured materials and the challenges associated with their synthesis can be addressed by chemists *via* skill manipulation. Often temperatures less than 300 °C are appropriate to operate in a Schlenk system in an advanced chemistry laboratory and the solvents and precursors can be degassed prior to or during an *in situ* stage. Sun *et al.*[67] and Wang *et al.*[68] dissolved Se powder in 1-octadecene (ODE) by heating and stirring it. The mixture of sodium molybdate, oleic acid (OLA) and octylamine was heated in an Ar atmosphere to obtain a red-brown solution. Later, they added ODE–Se solution to it and heated at ~300 °C for about half an hour. The SEM/EDAX and TEM analyses of the black

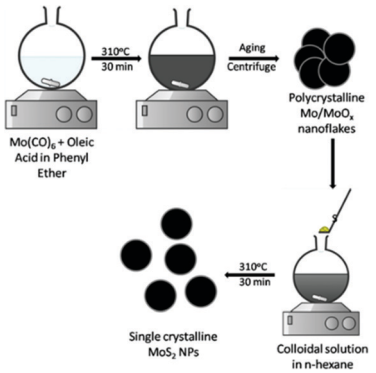

Fig. 9 Synthesis of ultra-small MoS_2 NPs using oleic acid.[66]

powder so obtained revealed formation of $MoSe_2$ nanoflowers consisting of nanosheets. Similarly, Zhang *et al.*[69] prepared a stock solution of Se in ODE and OLA. Sodium molybdate was dissolved in ODE and OLA and heated to 300 °C. The authors observed a colour change from light yellow to light brown and finally a clear dark brown solution. Subsequent addition of Se–ODE/Se–OLA solutions resulted in a black precipitate of nano-$MoSe_2$ clusters with a size of ~250 nm composed of ultrathin nanosheets as shown in the TEM images. EDAX analysis showed that these nanostructures were slightly Mo-rich. In a similar manner, Guo *et al.*[70] dissolved $Mo(CO)_6$ in oleylamine (OAm) to which they added Se–ODE precursor and heated the mixture at 200 °C for about half an hour. This way, ultrathin nanosheets of 2H-$MoSe_2$ were reported. Huang *et al.*[71] synthesised $MoSe_2$ nanoclusters having a particle diameter in the range of 3.5–6 nm. Synthesis employing chloride of molybdenum may however be really tricky and painstaking. The reaction takes a much longer time and thus increases the challenges for researchers. $MoCl_5$ was refluxed for three days in tetrachloroethylene in an inert atmosphere for reduction of $MoCl_5$ to $MoCl_4$. Subsequently, dissolving it in an inverse micelle solution of tri-dodecyl methylammonium iodide, hexanol and octane and combining with H_2Se yielded nanoclustered $MoSe_2$. It should be noticed that the use of H_2Se is not so convenient. To make the synthesis simpler, researchers have explored the use of organoselenium compounds as sources of selenium which avoids difficulties associated with the first stage of reaction where selenium precursors are generated *in situ*. Accordingly, Geng *et al.*[72] employed $MoO_2(acac)_2$ and $(PhCH_2)_2Se_2$ as precursors and OAm as the surfactant to synthesize $MoSe_2$ nanosheets. Thermally heating the mixture to ~250 °C yielded a black precipitate of thin sheet $MoSe_2$. Varied layers of $MoSe_2$ nanosheets were synthesized conveniently by Hassan *et al.*[73] by increasing the amount of surfactant during their experiment involving the use of $MoO_2(acac)_2$ in OAm, followed by heating with Se-precursor (prepared by stirring Se powder, OAm and 1-butanethiol) under an inert atmosphere. It was described that the reaction occurs *via* reduction of Se to Se^{2-} ions.

In line with $MoSe_2$, thermal methods are also effectively useful for synthesis of its tellurium counterpart. Thus, Sun *et al.*[74] were able to synthesize 1T′-$MoTe_2$ *via* a low-temperature thermal route by using TOPTe prepared by dissolution of Te powder in trioctylphosphine (TOP) and OAm by heating to obtain a yellow solution. Subsequent injection of hexamethyldisilazane along with $MoCl_5$ solution in OLA led to formation of a nanocrystalline product within half an hour at 300 °C. OLA was used as the complexing agent and OAm as the reducing reagent and HDMS was required for high crystallinity. 1T′-$MoTe_2$ nanoflowers were formed directly at this temperature instead of the more preferred and stable 2H polymorph. The authors suggested that this could be due to the low energy barrier for the 1T′ phase by the organic ligands. Qiu *et al.*[75] carried out a reaction between $Mo(CO)_6$ and Te powder in diphenylmethane by heating it for 24 h in a N_2 atmosphere. It was then annealed at 650 °C for 4 h to obtain $MoTe_2$ in a stoichiometric ratio. They observed that excess of Te was present in the sample before annealing. According to them, this was probably due to faster sublimation of $Mo(CO)_6$ and deposition of $MoTe_2$ particles over Te powder. SEM and TEM images indicated mixed morphologies in the form of nanorods and nanosheets. Liu *et al.*[76] synthesized nanosheets of 1T′-$MoTe_2$ with lateral dimensions of 250–350 nm and about 4 nm thickness. Te was first dissolved in TOP, then injected into $Mo(CO)_6$ dispersed in OAm and heated at more than 300 °C for 2 h. When the same experiment was repeated using $MoCl_5$, spherical nanostructures with smaller dimensions composed of defect rich nanosheets were observed. This states that different precursors can have different effects on the product morphology.

Chemical vapour deposition

Solid-state reactions mostly use MoO_3, sulphur, hydrogen, H_2S, *etc.* as precursors for the synthesis of nano-MoS_2 utilizing a high temperature tube furnace.[77–79] The temperature required to carry out solid-state reactions is very high to realize high yields and homogeneous quality, and to have precise control over layer numbers. CVD grown layers are prone to chalcogenide deficiency due to the volatile nature of chalcogens. Balendhran *et al.*[80] carried out a solid-state reaction between MoO_3 and S powder in a tube furnace which they referred to as the thermal evaporation technique using a quartz substrate in an argon environment. The reaction methodology for the same is shown in Fig. 10. It was demonstrated that layered MoS_2 deposition can be achieved *via* choosing the right combination of temperatures and durations. Highly crystalline and ordered layered structures were reported at an annealing temperature of 830 °C for 3 h. The suggested reaction mechanism is represented by eqn (17) and (18):

$$2MoO_3 + S \rightarrow 2MoO_2 + SO_2 \quad (17)$$

$$2MoO_2 + S \rightarrow 2MoO_2 + SO_2 \quad (18)$$

On the same line, Jeon and co-workers[81] synthesised monolayered MoS_2 with a controlled size of nanoparticles in the range of 5–60 nm by regulating the flow of hydrogen and argon. Here, they used a dual temperature zone furnace to carry out the reaction where sulphur powder was placed in the first zone and MoO_3 powder and the silicon substrate were placed next to each other in the second zone. Instead of one heating zone, two were preferred as sulphur is highly volatile than MoO_3, and to cause their evaporation at the same time, it is required to heat them at different temperatures. Otherwise, the product would be S-deficient as reported by several researchers where the reaction was carried out in a single zone. The setup of the

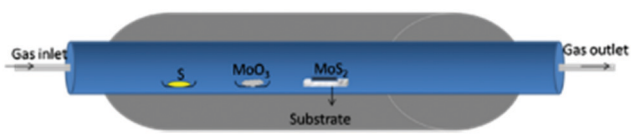

Fig. 10 Experimental setup for the reaction carried out in a tube furnace.[80]

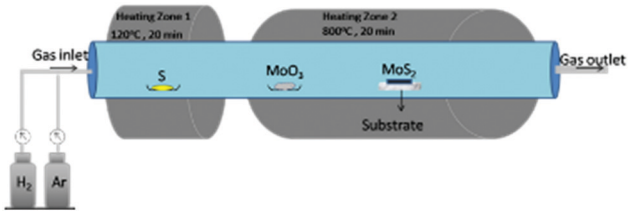

Fig. 11 Schematic diagram of the CVD system used to synthesise various sized MoS_2 nanoparticles by regulating the flow of gases.[81]

reaction is shown in Fig. 11. The first zone was heated at 120 °C and the second zone at 800 °C for 20 minutes with the ratio of Ar/H_2 well-regulated as required. The authors observed that the size of the nanoparticles can be reduced with increasing the H_2 flow rate. It is also worth mentioning that a typical MoS_2 stoichiometry was obtained when no hydrogen was used which the authors suggested could be due to the possible reduction of S, leading to substantial loss of sulphur during sulfurization of Mo. When MoS_2 is formed, the edges are covered by S dimers. As the flow of H_2 increases, it acts as the reducing agent and reacts with these surface-attached dimers to form H_2S. Therefore, instead of pure MoS_2, partially reduced $MoO_{3-x}S$ is deposited. The proposed reaction is represented by eqn (19) and (20):

$$H_2 + 0.5S_2 \rightarrow H_2S \quad (19)$$

$$MoO_3 + 3S + H_2 \rightarrow MoO_{3-x}S + SO_x + H_2 \quad (20)$$

Reacting MoO_3 nanobelts with sulphur powder, Li *et al.*[82] synthesised MoS_2 fullerenes. The reaction was performed in a tube furnace in an inert atmosphere of argon gas at a temperature higher than 800 °C.

Based on TEM analysis, the authors stated that nanotubes of MoS_2 as well as fullerene-like nanoparticles were formed by rolling of the layered structures. It is also evident from this article that the morphology of products is dependent on the morphology of the reactants. When the authors carried out the same reaction with micro MoO_3, nanoparticles of MoS_2 were formed instead of nanotubes. In an attempt to identify whether the formation of MoS_2 nanotubes from the reaction of MoO_3 with H_2S gas takes place through the MoS_3 intermediate,[83] Nath *et al.*[84] reported conversion of MoS_3 obtained by decomposition of ammonium thiomolybdate to MoS_2 nanotubes *via* heating it above 1200 °C in a hydrogen stream. Direct heating of ammonium thiomolybdate also yielded MoS_2 nanotubes. This indicates that MoS_3 is the intermediate in the formation of nanotubes. The reduction of ammonium thiomolybdate with hydrogen to produce MoS_2 *via* the MoS_3 intermediate is shown by eqn (21) and (22):

$$(NH_4)_2MoS_4 \rightarrow MoS_3 + H_2S + NH_3 \quad (21)$$

$$MoS_3 + H_2 \rightarrow MoS_2 + H_2S \quad (22)$$

Kong *et al.*[7] presented synthesis of thin MoS_2 and $MoSe_2$ layers vertically aligned on a substrate so as to achieve maximum catalytic activity. They obtained samples with an excellent arrangement of the layers as shown in the HRTEM images (Fig. 12). Recently, the use of KCl to obtain mixed phase MoS_2 heterostructures was also reported.[85]

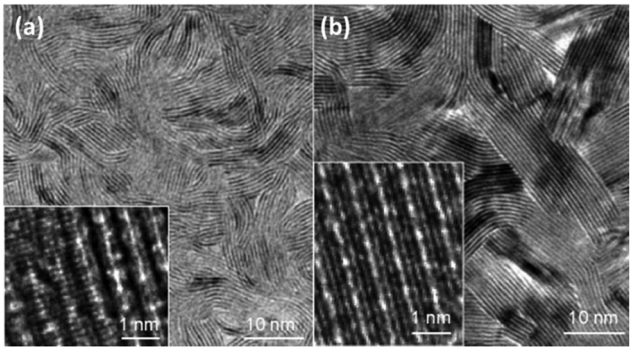

Fig. 12 TEM and the corresponding HRTEM (inset) images of (a) MoS_2 and (b) $MoSe_2$ depicting uniformly spaced and vertically aligned layers. Reprinted with permission from ref. 7 [D. Kong, H. Wang, J. J. Cha, M. Pasta, K. J. Koski, J. Yao and Y. Cui, *Nano Lett.*, 2013, **13**, 1341–1347]. Copyright 2013, American Chemical Society.

Lee *et al.*[86] prepared thin MoS_2 layers of ~0.72 nm thickness and more than 150 nm in lateral dimensions over an RGO coated Si/SiO_2 substrate *via* chemical vapour deposition taking MoO_3 and sulphur powder as precursors. The authors observed two prominent peaks at 627 and 677 nm in their PL spectra due to A_1 and B_1 direct excitonic transitions. Wypych *et al.*[87] carried out the reaction of potassium molybdate and H_2S by heating it for almost 24 h in the temperature range of 300–400 °C, followed by reduction in a H_2/N_2 atmosphere at a much elevated temperature (850 °C) for 3 days to form $KMoS_2$. After hydration and oxidation of $KMoS_2$, 1T′ MoS_2 was formed. The process took a very long time, and the product too contained some impurities. Modifying this process, Yu *et al.*[23] were successful to synthesise pure 1T′-MoS_2 crystals. After grinding K_2MoO_4 and S powder together, the mixture was annealed for 1.5 h at 450 °C under a H_2/Ar flow. Excess S was added to the obtained powder and again annealed for 10 h at 850 °C with increased H_2 flow, followed by soaking and washing with DI water. Later, it was soaked for a few hours in I_2/acetonitrile solution and dried after washing thoroughly with DI water to achieve 1T′-MoS_2 crystals. Replacing S with Se in this process, 1T′-$MoSe_2$ was prepared. Annealing 1T′-MoS_2 and 1T′-$MoSe_2$ at 200 °C produced 2H-MoS_2 and 2H-$MoSe_2$, respectively.

The higher negative reduction potential of Se poses greater challenges in the synthesis of $MoSe_2$ when compared with MoS_2.[88] Most reports on the synthesis of $MoSe_2$ layers use the CVD method in a very similar manner to the synthesis of MoS_2. Often selenization of MoO_3 with Se is a popular methodology to generate $MoSe_2$. It was demonstrated that Ar and N_2 are good carrier gases to maintain an inert atmosphere with some percentage of H_2 for facilitating reduction.[89–91] Shaw *et al.*[92] synthesised large triangular $MoSe_2$ monolayers having edge lengths up to 30 μm and heights up to 1 nm. The operating temperature of the furnace was kept at 750 °C for 15 minutes during which the zone

containing Se powder was maintained at ~300 °C to avoid faster vaporization of Se. Using the same method, Huang *et al.*[5] synthesised snow-like single crystal $MoSe_2$ with a hexagonal structure by use of Se and MoO_3 and placing a Si/SiO_2 substrate inverted over Se in a three-zone tube furnace. The reaction was carried out in an Ar/H_2 atmosphere, heating Se at 520 °C and MoO_3 at 820 °C for half an hour. Depending upon the gas flow rate, large triangular monolayers of lateral dimensions close to 20 μm and snow-like monolayers of 0.9 nm thickness were formed. The PL peak was observed at 814 nm corresponding to a 1.52 eV bandgap. The 2H-phase was confirmed from the SAED pattern and the *d*-spacing calculated matched [110] and [100] crystal planes.

Hanson *et al.*[93] transformed $MoSe_2$ from 2H to 1T′ *via* exposure to *n*-BuLi. They first synthesized 2H-$MoSe_2$ monolayers by the above-described CVD method by heating MoO_3 and Se powder at 800 °C. The chips were treated with *n*-BuLi solution in hexane for 12 h in an Ar atmosphere. Various characterization studies supported the successful formation of the 1T′-$MoSe_2$ monolayer. The PL spectra (Fig. 13) gave a bandgap value of ~1.5 eV for 2H-$MoSe_2$, while no photoluminescence was observed for 1T′-$MoSe_2$. Taking pointers from the synthesis of MoS_2 by reduction of the corresponding trisulphide,[84] Nath *et al.*[94] were successful in synthesizing $MoSe_2$ nanotubes in a similar manner. In addition, $MoSe_2$ nanotubes *via* decomposition of $(NH_4)_2MoSe_4$ in a reducing H_2 atmosphere were also successfully synthesized. The reaction involved is represented by eqn (23). The morphology of the products was analysed through TEM (Fig. 14).

$$(NH_4)_2MoSe_4 + H_2 \rightarrow MoSe_2 + 2H_2Se + 2NH_3 \quad (23)$$

Vikraman *et al.*[95] used a chemical bath deposition method to deposit $MoSe_2$ on the substrate and post-annealing at 450 °C for an hour. The bath solution in which the substrate was dipped contained AHM, SeO_2, N_2H_4, and NH_3 solution with a certain amount of HCl. They represented the overall reaction by eqn (24). The authors observed that with an increase in the deposition time, the thickness of the layers increased as expected. It was also noticed that the layers align vertically till the deposition time reached 15 minutes, and beyond that there was a random alignment of layers.

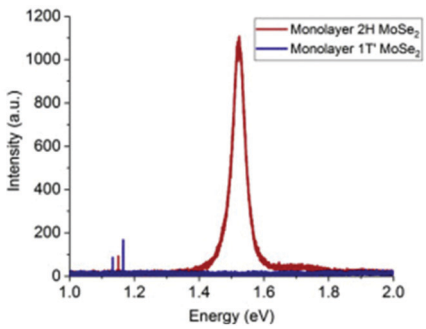

Fig. 13 PL spectra of monolayer 2H and 1T′-$MoSe_2$. Reprinted with permission from ref. 93 [E. D. Hanson, L. M. Lilley, J. D. Cain, S. Hao, E. Palacios, K. Aydin, C. Wolverton, T. Meade and V. P. Dravid, *Mater. Chem. Phys.*, 2019, **225**, 219–226]. Copyright 2019, Elsevier.

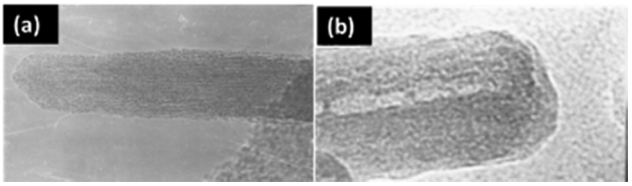

Fig. 14 $MoSe_2$ nanotubes obtained *via* decomposition of (a) $MoSe_3$ and (b) $(NH_4)_2MoSe_4$. Reprinted with permission from ref. 94 [M. Nath and C. N. Rao, *Chem. Commun.*, 2001, 2236–2237.]. Copyright The Royal Society of Chemistry.

$$\frac{1}{7}(NH_2)_6 \rightarrow Mo_7O_{24} + 2SeO_2 + \frac{1}{7}NH_3 + \frac{2}{7}N_2H_4MoSe_2 + NH_4OH + \frac{2}{7}N_2 + \frac{45}{14}O_2 \quad (24)$$

Gas phase reactions to synthesise $MoTe_2$ are not easily achievable as a consequence of a lower bonding energy between Mo and Te or the requirement of high temperatures and longer durations to react. Moreover, at higher temperatures, instead of forming $MoTe_2$ vapours, it loses Te as vapours leading to Te deficiency in the prepared $MoTe_2$ samples. The $MoTe_2$ layers being prone to oxidation are often coated with a protective layer of materials such as aluminium, polymethylmethacrylate (PMMA), silica, *etc.* Therefore, the synthesis of few-layer $MoTe_2$ is highly challenging. The melting point of Te is about 450 °C. A large number of articles have reported the use of the CVD method for $MoTe_2$ synthesis.[28,96–98] Huang *et al.*[31] used the physical vapour deposition technique to produce 3L 2H-$MoTe_2$. $MoTe_2$ was deposited on a silica substrate from a $MoTe_2$ target for half a minute at 400 °C in an inert environment using a DC magnetron sputtering system. Then, the sample was annealed for several hours at 650 °C in a N_2 atmosphere after coating it with a protective layer of silica, in an attempt to avoid decomposition of $MoTe_2$. The 1T′ phase transformed to the 2H phase post-annealing and the cross-sectional HRTEM image of $MoTe_2$ showed a three-layer stacked 2H-MoS_2 structure with 2.1 nm thickness.

Zhou *et al.*[99] and Hussain *et al.*[100] synthesised $MoTe_2$ *via* tellurization of MoO_3 and Mo films. Mo film was deposited on a SiO_2 substrate and converted to MoO_3 *via* oxidation in air. It was then placed over Te powder in a CVD chamber in a reducing environment of Ar/H_2 at 700 °C. Large nanosheets of ~30 μm lateral size were observed. The authors also mentioned that when a Mo film was used instead of the MoO_3 film, the 1T′ phase was obtained. In place of depositing the MoO_3 film directly from MoO_3 powder, the authors oxidised a Mo film to form MoO_3 because MoO_3 has a tendency to lose oxygen during evaporation. Similarly, in another experiment MoO_3, $MoCl_5$ and Te were taken in a 1 : 1 : 1 weight ratio and heated in a tube furnace at 780 °C for nearly 15 minutes, resulting in formation of 1T′-$MoTe_2$ monolayers.[101] Shirpay *et al.*[102] deposited nanosheets of 2H-$MoTe_2$ *via* the chemical vapour transport method

using MoO_3 and TeO_2. Kim and co-workers[103] were able to synthesize ultrathin $MoTe_2$ mixed phase films with a thickness of about 1–2 nm at a lower temperature using the $Mo(CO)_6$ complex and dibutyl telluride as the precursors. Pradhan *et al.*[104] synthesized bi-layered $MoTe_2$ crystals on a silica substrate using iodine as the transport agent. As starting materials, they utilized Mo and Te powders, which required a very high temperature (~1100 °C) and a very long duration (1.5 weeks) to react. Yang *et al.*[105] controlled the $MoTe_2$ nanosheet phases by optimizing the flow of the carrier gas employed and the tellurization temperature. The synthesis was carried out in a two-zone CVD chamber using MoO_3 and Te to obtain thin films with thickness around 4 nm. The four stages observed were the 2H phase dominant coexistence of both phases, pure 2H phase, 1T′ phase dominant coexistence of both phases and phase pure 1T′-$MoTe_2$. They observed that when the flow rate of N_2 was increased from 1 sccm (standard cubic centimeters per minute) to 40 sccm, the 1T′ dominant phase was transformed to the 2H dominant phase with phase pure 2H-$MoTe_2$ at 3 sccm and 1T′-$MoTe_2$ at approximately 90 sccm. The dependence of phase on the synthesis temperature was also studied and the authors suggested that achieving 100% pure 2H-$MoTe_2$ was highly unapproachable, while a pure 1T′ phase can be easily obtained with a high rate of tellurization. In a similar attempt to utilize $MoTe_2$ as a phase change material, Empante *et al.*[106] obtained 1T, 1T′ and 2H phases by varying the cooling rate of the furnace after the reaction. They carried out a reaction between MoO_3 and Te in a CVD chamber for about 30 min at 650 °C for the 2H phase and at 680 °C for the other two phases. 1T, 1T′ and 2H phases were obtained when the chamber was opened after the temperature reached below 450 °C, 350 °C and 100 °C, respectively. This suggested that the 2H-phase is favoured at lower temperatures and an increase in temperature maximises the probability of 1T-$MoTe_2$ formation.

In CVD, the film quality, *i.e.*, the dimensions and the stoichiometry, is dependent on the amount of solid precursors, the distance at which they are placed, the substrate and its position, growth temperature and duration. The cooling rates of the sample also determine the phase of MoX_2 compounds.

Microwave method

Microwave radiation causes direct and targeted heating of the sample with a minimum dissipation of energy in the surrounding. The use of microwave transparent glassware minimises the loss of energy to heat the sample container. Under microwave irradiation, solvents are superheated. As a result of this overheating, metal ions may reduce to a zerovalent state. Metal particles strongly interact with microwave irradiation, yielding very favourable reduction conditions. Microwave energy is more intense as compared to thermal heating and also there is targeted heating of the reaction mixture, thereby avoiding the energy wastage in heating a higher quantity of solvent and the reaction vessel which is generally the case in thermal heating. Therefore, microwave reactions are more efficient and less time-consuming. Qureshi *et al.*[107] synthesised biocompatible and non-cytotoxic MoS_2 by a microwave-assisted solvothermal method. AHM and elemental sulfur were taken in a 1 : 1 ratio in water, followed by addition of hydrazine monohydrate, for initial reaction activation. The reaction mixture was then irradiated with microwave radiation for 10 min at 270 W and the black precipitate suggested the formation of MoS_2. The authors observed the morphology of NPs to be elongated rod-shaped from TEM images, and the SEM images show stacked plate-like structures. The reaction schematic is shown in Fig. 15.

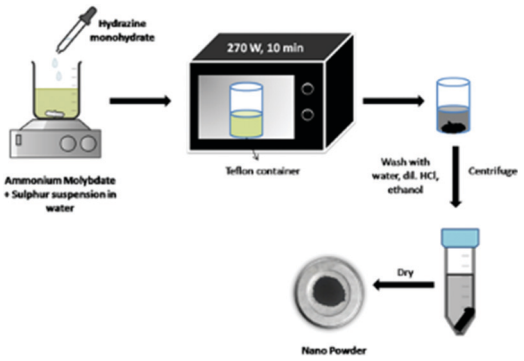

Fig. 15 Microwave synthesis of rod-shaped MoS_2 NPs.[107]

The polyol method is a potentially useful approach for the synthesis of metal NPs. Polyol serves as a reducing agent as well as a surface protecting agent. Harpeness *et al.*[108] utilised this method to synthesise $MoSe_2$ nanorods using a household microwave oven at 900 W, switched on for 21 s and off for 9 s to avoid overheating of the solvent and microwaved $Mo(CO)_6$ and Se mixture in ethylene glycol under an inert atmosphere. The black powder so obtained was further annealed at 600 °C for 5 h to obtain $MoSe_2$ with no impurities. The crystallite size obtained was within the 11–16 nm range consisting of nanorods 45–55 nm in length and diameter varying from 2.5 to 6 nm. The method is very much efficient and simple but still there are not many reports available on this. There are no reports on the synthesis of nanostructured $MoTe_2$ *via* this method. Therefore, the use of a household microwave oven is yet to be explored. It is expected to make the process simpler and more convenient.

Sono-chemical method

Uzcanga *et al.*[109] carried out the preparation of MoS_2 sonochemically using AHM and thiolacetic acid (CH_3COSH) in water by completely dissolving them and the reaction mixture thus generated was treated with sonication for 1 h at a high ultrasound intensity (20 kHz) and the black precipitate was annealed at 400 °C in a H_2/H_2S atmosphere for 4 hours. During sonication, water decomposes to produce hydrogen radicals which then produce H_2S gas on attacking thiolacetic acid acting as a sulfiding agent. Xu *et al.*[110] synthesised MoS_2 quantum dots (QDs) and nanosheets *via* a simple sonication method where MoS_2 in DMF was sonicated to exfoliate MoS_2. Following that, it was heated at 140 °C with stirring for several hours and then centrifuged to collect MoS_2 QDs from the supernatant and

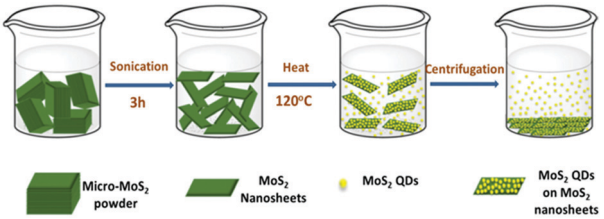

Fig. 16 Illustration of reaction steps for sonochemical synthesis of MoS_2 QDs and nanosheets. Reprinted with permission from ref. 110 [S. Xu, D. Li and P. Wu, *Adv. Funct. Mater.*, 2015, **25**, 1127–1136]. Copyright WILEY-VCH Verlag GmbH & Co. KGaA, Weinheim.

QD and nanosheet mixture *via* centrifugation. The overall synthetic approach is depicted in Fig. 16.

Kristl *et al.*[111] synthesised nanocrystalline $MoSe_2$ *via* a simple sono-chemical approach. The $Mo(CO)_6$ and Se mixture in decalin was prepared in a sono-chemical reaction vessel. This slurry was then irradiated with high-intensity ultrasound for several hours under N_2. The reaction temperature was maintained at 0 °C using a cooling bath. Amorphous $MoSe_2$, thus formed, was then annealed at 330 °C for 12 h to obtain nanocrystalline $MoSe_2$ spherical particles of 15–60 nm size analysed through TEM (Fig. 17(a)). The authors here commented on the very crucial role of temperature. The temperature of the reaction can reach up to 80 °C under these conditions and the rate of sono-chemical reactions decreases with an increase in temperature. When they kept the temperature of the water bath at 20 °C, there was an excess of Se in $MoSe_2$ compared to the stoichiometric ratio. They found it to be because of unreacted $Mo(CO)_6$ that sublimed and deposited on the walls before it could react with Se.

Yuwen *et al.*[112] synthesized $MoSe_2$ nanodots (NDs) from bulk $MoSe_2$ by ultrasonication using the triblock copolymer F-127, which gets absorbed on the surface of $MoSe_2$ particles and thereby offers water dispersibility. First, F-127 was dissolved in water to obtain a clear solution, followed by addition of $MoSe_2$ and stirring for some time. This solution was then sonicated for 4 h in an ice bath with a 2 s on/off cycle at a high power. The authors adopted gradient centrifugation to separate $MoSe_2$ NDs from larger particles. 2H-$MoSe_2$ NDs of size in the range of 2–3 nm and thickness of up to three layers were obtained after 3–4 cycles of centrifugation. In another report, $MoSe_2$ nanodots were retrieved from bulk-$MoSe_2$ *via* ultrasonication, conjugated with folic acid (FA) and stabilized by protein molecules. The corresponding XRD spectrum is shown in Fig. 17(b). Two peaks were observed at 700 and 800 nm in the absorbance spectra indicating a bandgap of 1.5–1.7 eV.[113]

In the synthesis of $MoTe_2$, $Mo(CO)_6$ was used as the precursor. The suspension of $Mo(CO)_6$ and tellurium powder was sonicated for 4 h in an Ar atmosphere, followed by drying and calcination. First, they observed formation of a mixture of nanosheets and nanotubes which upon calcination transformed to nanotubes due to rolling of nanosheets. The nanotubes of 20–50 nm diameter and of length 100–500 nm were observed in the HRTEM images (Fig. 17c) with a *d*-spacing of 0.345 nm for the (004) plane of monoclinic $MoTe_2$.[114] The XRD also supported the formation of monoclinic $MoTe_2$.

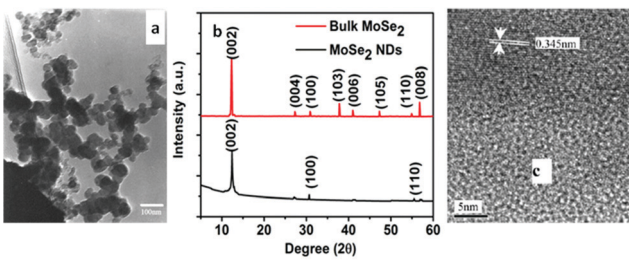

Fig. 17 (a) TEM image of spherical $MoSe_2$ NPs prepared sono-chemically. Reprinted with permission from ref. 111 [M. Kristl and M. Drofenik, *Inorg. Chem. Commun.*, 2003, **6**, 68–70]. Copyright Elsevier. (b) XRD pattern of $MoSe_2$ nanodots and its comparison with bulk $MoSe_2$. Reprinted with permission from ref. 113 [F. Qi and R. Liu, *Nanoscale Res. Lett.*, 2019, **14**, 67]. Copyright The Authors. (c) HRTEM image of $MoTe_2$ indicating the interplanar distance. Reprinted with permission from ref. 114 [L. Qiu, V. G. Pol, Y. Wei and A. Gedanken, *J. Mater. Chem.*, 2003, **13**, 2985]. Copyright The Royal Society of Chemistry.

Mechanical exfoliation

The process to peel off the atomically thin layer of a compound from its parent bulk crystals by micromechanical cleavage is called mechanical exfoliation. As MoX_2 are layered materials held together by weak forces, atomically thin layers can easily be peeled using Scotch tape. These cleaved thin layers on the Scotch tape are normally placed on a substrate and can be transferred *via* rubbing carefully. The monolayer and multilayer nanosheets can thus be isolated once the Scotch tape is peeled off. Silicon oxide with a thickness of 200–300 μm is generally the substrate of choice.[12,115–117] The method requires mild conditions, but the yield is very low. Additionally, there is little control over the number of layers being produced. In an attempt to resolve this, Dicamillo *et al.*[118] used a rheometer as an automated tool for mechanical exfoliation and obtained few-layer flakes of MoS_2 and $MoTe_2$. This automation offers reproducibility and adds to the efficiency of this technique. Here, a Nitto Blue tape was used instead of the regular Scotch tape as the amount of residue left on the substrate was less. The only disadvantage of this procedure is a low yield; however, researchers prefer this method as it produces MoS_2 layers of few micrometers thickness. Wafer anodic bonding was another modified method that promised a higher yield where one side of Pyrex glass was made anodic by placing pristine MoS_2 and the other side was made cathodic. It was then subjected to a voltage of 200–1500 V at a temperature of 130–200 °C and an adhesive tape was used to mechanically peel off the flakes and transfer the thin film on the substrate.[119] Tongay *et al.*[120] exfoliated monolayer MoS_2 and $MoSe_2$ on a 90 nm SiO_2 substrate and studied the effect of layer thickness and temperature on the PL intensity. In bulk, the bandgap of $MoSe_2$ is 1.1 eV, and therefore weak PL emission is expected. Splendiani *et al.*[117] also observed increased photoluminescence with a lower number of layers (emission peaks at 627 and 677 nm) which were absent in bulk MoS_2. The increased PL emission in the

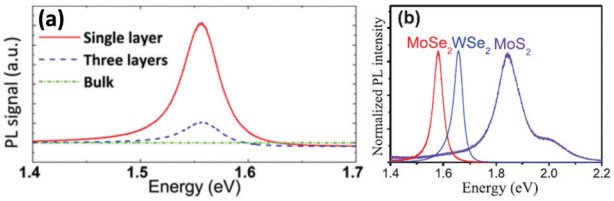

Fig. 18 PL spectra showing (a) thickness dependence in $MoSe_2$. Reprinted with permission from ref. 27 [S. Tongay, J. Zhou, C. Ataca, K. Lo, T. S. Matthews, J. Li, J. C. Grossman and J. Wu, *Nano Lett*, 2012, 12, 5576–5580]. Copyright 2012 American Chemical Society. Comparison of (b) mono-layered MoS_2 and $MoSe_2$. Reprinted from ref. 134 [M. Yang, X. Cheng, Y. Li, Y. Ren, M. Liu and Z. Qi, *Appl. Phys. Lett.*, 2017, **110**, 093108] with the permission of AIP Publishing.

single layer compared to multi-layer one was attributed to the indirect-to-direct bandgap crossover due to quantum confinement in the perpendicular direction. The PL intensity generally decreases for semiconductors with an increase in temperature as non-radiative processes are enhanced.[120] Similar observations were observed for monolayer and few-layer MoS_2 and few-layer $MoSe_2$ but contradictory results were observed for single-layer $MoSe_2$ (Fig. 18(a)).[27] Several authors have reported the synthesis of $MoSe_2$ *via* mechanical exfoliation.[26,121,122] Similarly, for preparation of nanocrystalline $MoTe_2$, Ruppert *et al.*,[32] Feng *et al.*[123] and several other researchers also adopted the same method.[124–133] In Fig. 18(b), the PL spectra of the MoS_2 and $MoSe_2$ monolayers synthesized by mechanical exfoliation are shown. Strong PL emission was observed at 1.56 eV and 1.85 eV for $MoSe_2$ and MoS_2, respectively.[134] Yu *et al.*[23] also reported the PL spectroscopy results of 1T′-MoS_2 and 2H-MoS_2 obtained by thermal annealing of 1T′-MoS_2 (Fig. 19(a)). 1T′-MoS_2 did not show PL emission; however, 2H-MoS_2 has shown strong photoluminescence at about 670 nm which is probably due to interlayer interactions and spin–orbit coupling. Li *et al.*[135] in their review article have discussed the relation of the PL bands to the number of layers. As the photoluminescence falls in the visible region, this property can be utilised for

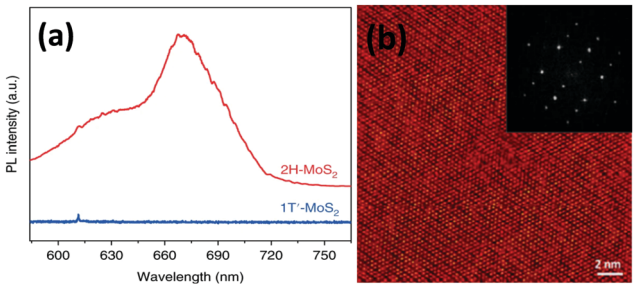

Fig. 19 (a) PL spectra of 1T′ and 2H-MoS_2.[23] Reprinted with permission from Springer Nature [Y. Yu, G. H. Nam, Q. He, X. J. Wu, K. Zhang, Z. Yang, J. Chen, Q. Ma, M. Zhao, Z. Liu, F. R. Ran, X. Wang, H. Li, X. Huang, B. Li, Q. Xiong, Q. Zhang, Z. Liu, L. Gu, Y. Du, W. Huang and H. Zhang, *Nat Chem*, 2018, **10**, 638–643] Copyright 2018, The Authors. (b) STEM image of 1T′-MoS_2 (inset – Fourier transformed STEM image). Reprinted with permission from ref. 25 [C. Guo, J. Pan, H. Li, T. Lin, P. Liu, C. Song, D. Wang, G. Mu, X. Lai, H. Zhang, W. Zhou, M. Chen and F. Huang, *J. Mater. Chem. C*, 2017, **5**, 10855–10860]. Copyright The Royal Society of Chemistry.

various applications such as photocatalysis, photonic devices, *etc.* The foremost shortcoming of this method is the production of small and arbitrary shaped flakes distributed over a surface, thus forbidding their use in large-scale applications.

Chemical exfoliation

Chemical exfoliation overcomes the low-yield problem of mechanical exfoliation. It includes two approaches involving ion intercalation and solvent exfoliation. The ion intercalation method includes the insertion of small ions between the gaps of layers increasing the space between the layers. Then, these intercalated layers are reacted with water or some solvent like ethanol or methanol. Hydrogen gas is evolved during hydrolysis of ions and separates layers in single sheets suspended in the solvent. Mostly Li ions are used for intercalation due to their small size.[136] The amount of lithium intercalated decides the phase purity of the material. Lin *et al.*[137] used *n*-BuLi (*n*-butyl lithium) for exfoliation of layers from bulk MoS_2. *n*-BuLi in hexane was added to MoS_2 and sealed in an autoclave which was heated at 80 °C for 4 h. The dried Li_xMoS_2 thus formed was hydrolyzed and sonicated for some time to obtain a colloidal suspension of MoS_2 layers. In another report, ultrathin 1T′-MoS_2 nanosheets were exfoliated from micro-MoS_2 using Li_2S. A mixture of MoS_2, Li_2S and Mo powders was taken in a quartz tube, sealed and heated to 800 °C for 10 h. The thus-obtained $LiMoS_2$ powder was shaken in water for 12 h, which resulted in a colloidal solution of MoS_2 nanosheets, and the 1T′ phase was confirmed by STEM (Fig. 19(b)).[25] Although the low-yield problem of the mechanical exfoliation method gets resolved to some extent, the control over size and thickness gets reduced. Additionally, expensive reagents are required, and the problem of Li-ion toxicity exists. Impurities are easily introduced as the Li_xMoX_2 compounds are highly air sensitive, thereby requiring extensive cleaning which hampers the yield and may even cause structural destruction.

Pulsed laser ablation

The pulsed laser ablation (PLA) method is extensively used for the preparation of NPs. In this process, a laser beam is used as the primary excitation source for the vaporisation of the metal precursor from the surface. A high energy pulsed laser beam hitting the target material generates high temperatures which vaporize the substance quickly. The wavelength and duration of the pulse (Hz), and laser ablation time are chosen depending upon the material to be synthesised. Han *et al.*[138] synthesised MoS_2 NPs *via* the PLA method where a MoS_2 pellet was fixed at the bottom of a quartz tube in PVP solution and ablated for 10 min with continuous stirring using a Nd:YAG pulsed laser (10 Hz, 532 nm, and 100 mJ). The SEM images showed spherical nanoparticles (NPs), while TEM images revealed a layered structure. Likewise, Wu *et al.*[139] synthesized $MoSe_2$ IFs by ablation of the $MoSe_2$ pellet in ethanol/water solution for 3 minutes using a Nd:YAG pulsed laser (10 Hz, 532 nm, and 300 mJ). Spherical NPs of 20 nm size were observed in SEM and TEM.

Analysis of phases and layer numbers

Raman spectroscopy

Raman spectroscopy is a reliable and non-destructive method to study lattice vibrations and phonon modes in materials. The Raman study becomes crucial when dealing with layered compounds. It is a very definitive tool to determine the number of layers in the synthesized samples. As MoX_2 compounds exist in different phases, semiconducting as well as metallic, Raman spectroscopy is also the most convenient tool to identify these phases. Almost every report on synthesis of MoX_2 compounds has mentioned the use of Raman spectroscopy for characterization. Kong *et al.*[7] analysed the as-synthesized MoS_2 using Raman spectroscopy where they observed two peaks for the E^1_{2g} and A^1_g modes at approximately 380 cm^{-1} and 420 cm^{-1}, respectively. Late *et al.*[12] synthesized monolayer MoS_2 whose Raman spectrum was then compared with that of bulk MoS_2. Fig. 20(a) shows the out-of-plane A^1_g and in-plane E^1_{2g} mode position in the Raman analysis of monolayer MoS_2 and compares with the peak positions in the bulk form. Byrley *et al.*[140] photochemically induced a 2H to 1T phase transition in MoS_2 and monitored by Raman spectroscopy. The appearance of additional peaks at 330 and 370 cm^{-1} confirms the 1T phase and a distance of $\sim$20 cm^{-1} between E^1_{2g} and A^1_g peaks indicated a MoS_2 monolayer. Baledharan *et al.*[80] reported that as the number of layers decreases, the intensity of the Raman peaks decreases. It has been reported that the distance between the out-of-plane A^1_g or B^1_{2g} and in-plane E^1_{2g} peaks is indicative of the number of layers and decreases when the thickness of the films increases.[27] For example, a gap of almost $\sim$18 cm^{-1} indicates monolayer MoS_2.[86] Guo *et al.*[25] very qualitatively represented the phase transformation in MoS_2 through the Raman spectra of primitive (1T′-MoS_2), mixed phase and 2H-MoS_2 (Fig. 20(b)). Peaks at 156, 228, 283, 330, 403 cm^{-1} were obtained for 1T′-MoS_2. The non-appearance of any peak at 383 cm^{-1} indicates the absence of the 2H counterpart.

The doublet in the range of 380–420 cm^{-1} is characteristic of 2H-MoS_2.[141] Although most of the reports support that blue and red shifts are observed in the A^1_g and E^1_{2g} peaks, resulting in a decreased peak distance,[142] there are a few studies which report divergent behaviour. For instance, Zhu *et al.*[143] observed Raman frequencies at 379.6 and 401.8 cm^{-1} for 4 nm thickness, blue-shifted from the pristine MoS_2. The reason provided by them was the distortion in the structure due to intercalating ion induced strain. Thanh *et al.*[144] reported a blue shift in the Raman peaks (Fig. 20(c)) when MoS_2 layers of 1.5 to 3.5 nm thickness were produced *via* N_2 quenched exfoliation. The peak distance however decreased, consistent with other reports. Yang *et al.*[145] observed blue and red shifts in both the Raman peaks upon inducing strain in the plane and out of the plane, respectively.

2H-$MoSe_2$ shows 12 modes of vibration, of which A^1_g, E^1_g, E^1_{2g}, and E^1_{2g} are Raman active. As shown in Fig. 20(d), the out-of-plane A^1_g is the more prominent peak at about 240 cm^{-1} and the peak at 280 cm^{-1} is reported to be due to the E^1_{2g} in-plane mode of vibration.[27] A peak at around 350 cm^{-1} due to the interlayer

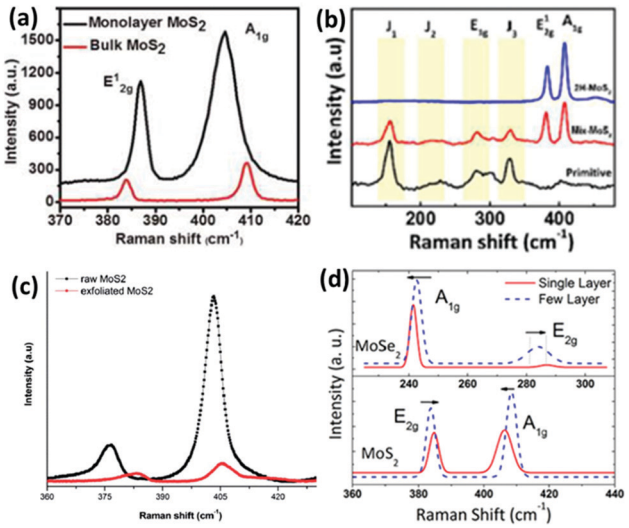

Fig. 20 (a) Raman spectra showing comparison between the phonon mode positions in bulk and monolayer MoS_2. Reprinted with permission from ref. 12 [D. J. Late, B. Liu, H. S. Matte, V. P. Dravid and C. N. Rao, *ACS Nano*, 2012, **6**, 5635–5641]. Copyright 2012 American Chemical Society. (b) Raman spectra of various phases. Reprinted with permission from ref. 25 [C. Guo, J. Pan, H. Li, T. Lin, P. Liu, C. Song, D. Wang, G. Mu, X. Lai, H. Zhang, W. Zhou, M. Chen and F. Huang, *J. Mater. Chem. C*, 2017, **5**, 10855–10860]. Copyright The Royal Society of Chemistry. (c) Blue shift in Raman peaks observed for exfoliated MoS_2. Reprinted with permission from ref. 144 [D. Van Thanh, C.-C. Pan, C.-W. Chu and K.-H. Wei, *RSC Adv.*, 2014, **4**, 15586–15589]. Copyright The Royal Society of Chemistry. (d) Thickness dependence of the Raman spectra of MoS_2 and $MoSe_2$[27] [S. Tongay, J. Zhou, C. Ataca, K. Lo, T. S. Matthews, J. Li, J. C. Grossman and J. Wu, *Nano Lett.*, 2012, **12**, 5576–5580]. Copyright 2012 American Chemical Society.

interaction is also considered as a characteristic peak which is absent in monolayer $MoSe_2$.[134]

Likewise, Raman spectroscopy is also often used to identify various phases of $MoTe_2$ where the 2H-phase exhibit peaks at 119, 171, 233 and 289 cm^{-1} corresponding to in-plane E_{1g}, out-of-plane A_{1g}, in-plane E^1_{2g} and out-of-plane B^1_{2g} modes, of which the peak at 233 cm^{-1} was the most prominent.[99,106] In another report, the peaks at 171.4 (A_{1g}), 234.7 (E^1_{2g}), and 290.0 cm^{-1} (B^1_{2g}) corresponded to the major Raman vibrational modes of 2H-$MoTe_2$.[29] It is also reported that the thickness of the $MoTe_2$ layers can be determined by the intensity ratio of the B^1_{2g} and E^1_{2g} peaks, *e.g.* a decrease in the ratio means an increase in the number of layers. In the case of the 1T′-phase of $MoTe_2$, it has been reported that the chalcogenide layer is slightly offset compared to other phases, resulting in a distorted structure which gives rise to a higher number of Raman peaks compared to the 2H-phase. Empante *et al.*[106] observed Raman peaks at 80, 85, 102, 112, 126 and 162 cm^{-1} for the 1T′-phase and some additional peaks at 189 and 257 cm^{-1} were also reported by Zhou *et al.*[99] Generally, the broad peaks at 155 and 242 cm^{-1} can be related to the 1T-phase of $MoTe_2$.[106]

Few-layer $MoTe_2$ shows also a characteristic out-of-plane B^1_{2g} peak which is normally absent in monolayer and bulk $MoTe_2$. Also, the peak at about 255 cm^{-1} for multilayer $MoTe_2$ can be

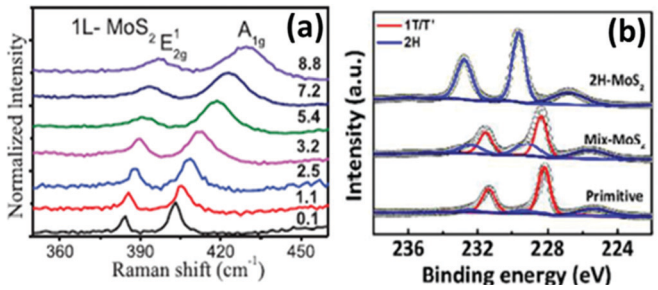

Fig. 21 (a) Raman spectra of MoS_2 pressure dependence on Raman modes. Reprinted from ref. 134 [M. Yang, X. Cheng, Y. Li, Y. Ren, M. Liu and Z. Qi, *Appl. Phys. Lett.*, 2017, **110**, 093108] with the permission of AIP Publishing. (b) XPS spectra of 2H-MoS_2, the 2H/1T′ mixture and 1T′-MoS_2 (primitive). Reprinted with permission from ref. 25 [C. Guo, J. Pan, H. Li, T. Lin, P. Liu, C. Song, D. Wang, G. Mu, X. Lai, H. Zhang, W. Zhou, M. Chen and F. Huang, *J. Mater. Chem. C*, 2017, **5**, 10855–10860]. Copyright The Royal Society of Chemistry.

tuned and a blue shift for the monolayer may be realized.[160] Table 3 summarises the Raman peak values of MoX_2 from various reports. However, these values may vary from report to report as the peak positions are phase and thickness dependent. Fig. 20(d) shows a representation of the effect of layer thickness on the Raman peaks of MoS_2 and $MoSe_2$.[27] It is also well known that the Raman peak values are dependent upon the wavelength of laser light used.[122] Yang *et al.*[134] studied the variations in the Raman frequencies of MoS_2 and $MoSe_2$ with temperature and pressure. Fig. 21(a) shows that the peaks are blue-shifted on increasing pressure. However, a red shift was observed by the authors when the temperature was increased. Inter-atomic interactions are enhanced when the pressure is increased causing compression of the out-of-plane mode leading to broadening of the A_{1g} peak in comparison to the E^1_{2g} peak. Similarly, with an increase in temperature, the kinetic energy increases. Therefore, inter-atomic interactions are diminished, and a red shift was observed.

X-Ray photoelectron spectroscopy (XPS)

XPS is another important tool to obtain useful information about the bonding, structure/phases and morphology of these compounds. The CVD method generally involves the use of MoO_3 as the Mo precursor, and the extent of reaction completion can be estimated from the XPS spectra. Molybdenum is present as Mo^{+6} in MoO_3 and shows binding energies of 232.5 and 235.9 eV for $3d_{5/2}$ and $3d_{3/2}$, respectively, while these values are much lower in respective chalcogenides.[5] The typical binding energies of various elements in MoX_2, *e.g.* Mo, S, Se and Te, are listed in Table 4. Fig. 21(b) shows the binding energy

Table 2 Comparison of the synthesis methods, properties and performance of molybdenum dichalcogenides in various applications

Method	Nanomaterial	Morphology and properties	Application	Performance	Ref.
Hydrothermal	2H-MoS_2, 2H-$MoSe_2$	Average size ~ 4 nm, average size ~ 7 nm,	—	—	146
	2H-MoS_2	λ_{abs} ~ 450, 618 and 665 nm, bi-layer with a lateral size of ~200 nm^{-1} μm	p-Si/n-MoS_2 photodetectors Photocatalysis	Rectification ratio of 1000 order Rhodamine B degradation	147
	MoS_2 QDs	Size ~ 8 nm	Atrazine aptasensors based on MoS_2 QDs/TiO_2 nanotubes	Detection limit up to 1 pM	148
	MoS_2	Nanoflowers with a size of about 300 nm composed of nanosheets	Supercapacitors	Specific capacitance – 122 F g^{-1} at 1 A g^{-1}	149
	2H-MoS_2	Nanoflowers	Supercapacitors	Specific capacitance – 106 F g^{-1}	150
	2H/1T-$MoSe_2$	Nanoflowers composed of nanosheets: specific surface area – 38.14 m^2 g^{-1} and specific pore volume – 0.17 cm^3 g^{-1}	Full spectrum absorption	—	151
	2H/1T-$MoSe_2$	Few-layer nanosheets: λ_{abs} ~ 440, 500, 705 and 800 nm, surface area – 23 m^2 g^{-1}	HER	Tafel slope ~ 75 mV dec^{-1}	56
Solvothermal	2H-$MoSe_2$ by use of olive oil as a surfactant	Mono-bilayer with 500 nm lateral dimensions, λ_{abs} ~ 672 and 791 nm, λ_{em} ~ 376.6 nm; E_g = 0.83 eV	Photodetectors	Response time ~ 8 s, external quantum efficiency ~ 50%	152
Thermal	2H-$MoSe_2$	Nanoflowers ~ 400 nm	HER	Overpotential ~ 230 mV, Tafel slope ~ 82 mV dec^{-1}	153
Microwave	$MoSe_2$	Spherical nanoparticles and nanorods: crystallite size – 11–16 nm	—	—	154
	2H-$MoSe_2$	Mesoporous dry-leaf like morphology: specific surface area – 64.63 m^2 g^{-1}	HER and supercapacitors	Tafel slope ~ 82 mV dec^{-1}, specific capacitance – 257.38 F g^{-1} at 1 A g^{-1}	155
CVD	MoS_2	Triangular monolayers with a lateral size of 10–50 μm	Photodetectors	Photoresponsivity – 2.5 × 10^4 A W^{-1}, specific detectivity – 4.1 × 10^{14} Jones	156
	$MoSe_2$		Photodetectors	Photoresponsivity – 859 mA W^{-1}, specific detectivity – 1.55 × 10^{11} Jones, response time ~38 ms	157
Liquid exfoliation	MoS_2	Thickness <10 layers with lateral dimensions of up to 90 nm, λ_{abs} ~ 610, 669 nm	HER	Overpotential ~ 420 mV, Tafel slope ~ 41 mV dec^{-1}	158
Mechanical exfoliation	$MoSe_2$	λ_{em} ~ 780 nm, average decay time ~ 1.08 ns	Photodetectors	—	159

Table 3 Typical Raman values for MoX_2 (X = S, Se, Te)

Material	Raman active modes	Raman frequency (cm^{-1})	Ref.
MoS_2	E^1_{2g}	385.8	86
	A_{1g}	403.8	
2H-MoS_2 (monolayer)	E^1_{2g}	382.3	134
	A_{1g}	402.1	
2H-MoS_2 (multilayer)	E^1_{2g}	381	80
	A_{1g}	406	
2H-MoS_2(mono/bilayer)	E^1_{2g}	380	161
	A_{1g}	404	
2H-$MoSe_2$	E^1_{2g}	283.8	52
	A_{1g}	239.9	
2H-$MoSe_2$	E^1_{2g}	284.9	5
	A_{1g}	239.7	
2H-$MoTe_2$	A_{1g}	171.4	29,162
	E^1_{2g}	234.7	
	B^1_{2g}	290.0	
1T′-$MoTe_2$	B_g	163	29,162
	A_g	262	
1T′-$MoTe_2$ (monolayer)	Ag	112	160,163
		127	
		161	
		252	
		269	
2H-$MoTe_2$ (few-layer)	E_{1g}	119	99
	A_{1g}	171	
	E^1_{2g}	234	
	B^1_{2g}	289	
1T′-$MoTe_2$	A_u	107	99,164
	A_g	126.9	
	B_g	163	
	A_g	256.1	

Table 4 Typical binding energies of the corresponding elements in MoX_2 compounds

	Peaks (binding energy)					
Material	$Mo3d_{5/2}$	$Mo3d_{3/2}$	$Te3d_{5/2}$		$Te3d_{3/2}$	Ref.
2H-$MoTe_2$	228.2	231.4	572.9		583.3	29
2H-$MoTe_2$	228.3	—	572.9		—	162
1T-$MoTe_2$	227.7	231.0	572.1		582.5	160
	$Mo3d_{5/2}$	$Mo3d_{3/2}$	$Se3d_{5/2}$		$Se3d_{3/2}$	
2H-$MoSe_2$	229	232	54.4		55.3	52
2H-$MoSe_2$	229.5	232.9	55.5		56.4	166
2H-$MoSe_2$	229.7	232.8	54.7		55.4	5
2H-$MoSe_2$	229.0	232.1	—		—	23
1T′-$MoSe_2$	228.1	231.2	—		—	23
	$Mo3d_{5/2}$	$Mo3d_{3/2}$	$S2p_{3/2}$	$S2p_{1/2}$	S2s	
2H-MoS_2	229.1	232.1	161.25	162.94	226.25	43
2H-MoS_2	229.1	232.2	—	—	226.1	23
2H-MoS_2	229.6	232.7	162.4	163.6	—	81
1T′-MoS_2	228.2	231.3	—	—		25
1T′-MoS_2	228.3	231.4	—	—	225.3	23
MoS_2	229.3	232.4	—	—	—	66

position and shift in peaks on transforming the phase. The binding energies are slightly higher for the 2H-phase than for 1T′-MoS_2. The peaks for Mo^{+4} for MoS_2 in the 2H phase appear at around 230 and 233 eV which shift to a lower energy transformation of the semiconducting phase to the metallic phase.[25] Byrley *et al.*[140] observed similar phenomena where the broadening in the peaks indicated a mixture of both the phases with peaks at 230 and 233 eV shifted to lower energies. Wang *et al.*[165] reported a peak shift in Mo($3d_{5/2}$) and S(2p) in MoS_2 nanoparticles by +1.6 eV and −2.2 eV, respectively, in comparison to elemental Mo and S because of partial electron transfer from the Mo metal to the chalcogen owing to the greater electronegativity of S than Mo. As a result, Mo gains a partial positive charge which is reflected by the increase in binding energy and sulfur gains a negative charge, hence a decrease in binding energy.[43]

X-Ray diffraction (XRD) technique

XRD patterns give a clear indication of the phase of MoX_2 compounds with measurement of the cluster size and also provides information on lattice spacings. The XRD peak positions for 2H-MoS_2 are reported to be around 2θ ~14°, 32.7°, 33.5°, and 58.3° prominently due to the [002], [100], [101] and [110] planes, respectively.[46,60,80,86] The peak at 2θ = 14° is the most intense one in MoS_2 and can give information about the phase and the number of layers as it varies marginally even with slight changes in the structure and morphology. It is reported that the absence of a peak at 2θ = 14.4° is a typical characteristic of monolayer MoS_2.[43] Similarly, the peak at about 14.8°, typical for 1T′-MoS_2, may shift to lower angles (~14.4°) when transformed to the 2H phase (Fig. 22(a)).[23] Other Mo-chalcogenides show similar behaviour, *e.g.* an almost 0.3° variation has been shown in the case of 1T′ and 2H-$MoSe_2$ for the peak at ~13.9° (Fig. 22(b)).[23]

Atomic force microscopy (AFM)

AFM is a conclusive tool to estimate the number of layers/thickness of the deposited materials. Dividing the height of the as-synthesized layers by the thickness of one layer gives a good estimation of the number of layers present in the as-synthesized material.[110,161] Zhou *et al.*[99] found the height of the as-prepared $MoTe_2$ through AFM to be approximately 3.1 nm. The interlayer

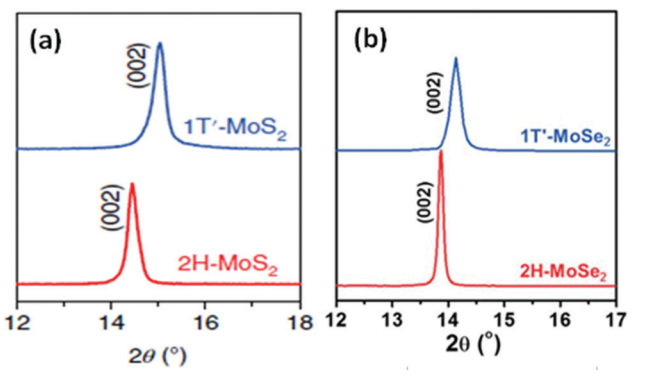

Fig. 22 Variation in XRD peaks depending upon the phase of the (a) MoS_2 and (b) $MoSe_2$ compounds. Reprinted with permission from ref. 23 [Y. Yu, G. H. Nam, Q. He, X. J. Wu, K. Zhang, Z. Yang, J. Chen, Q. Ma, M. Zhao, Z. Liu, F. R. Ran, X. Wang, H. Li, X. Huang, B. Li, Q. Xiong, Q. Zhang, Z. Liu, L. Gu, Y. Du, W. Huang and H. Zhang, *Nat. Chem.*, 2018, **10**, 638–643.]. Copyright 2018, The Author(s).

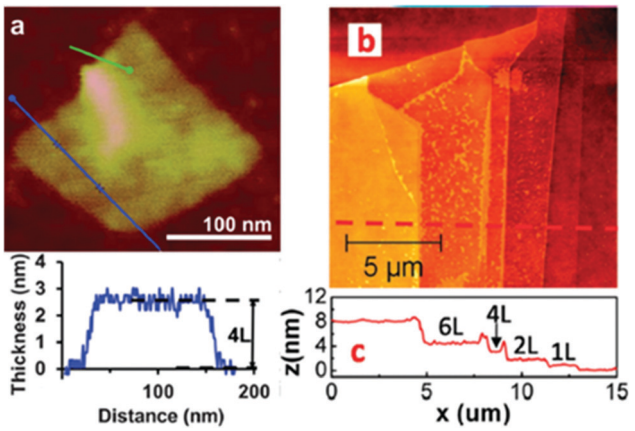

Fig. 23 AFM image of (a) CVD grown (reprinted with permission from ref. 80 [S. Balendhran, J. Z. Ou, M. Bhaskaran, S. Sriram, S. Ippolito, Z. Vasic, E. Kats, S. Bhargava, S. Zhuiykov and K. Kalantar-Zadeh, *Nanoscale*, 2012, **4**, 461–466], Copyright The Royal Society of Chemistry) and (b) mechanically exfoliated MoS_2 flakes with the height profile along the red line. Reprinted with permission from ref. 117 [A. Splendiani, L. Sun, Y. Zhang, T. Li, J. Kim, C. Y. Chim, G. Galli and F. Wang, *Nano Lett.*, 2010, **10**, 1271–1275]. Copyright 2010 American Chemical Society.

spacing of $MoTe_2$ is about 0.7 nm, and therefore a four-layer $MoTe_2$ film was formed. Fig. 23 shows the AFM image of the MoS_2 flakes obtained from CVD and mechanical exfoliation methods.[80,117] The interlayer spacings for MoS_2, $MoSe_2$, and $MoTe_2$ are 0.615, 0.646 nm[167] and 0.691 nm,[76] respectively. Therefore, the film thickness divided by interlayer spacing gives the number of layers of MoS_2. The figures display multilayer formation at different positions in the sample. Similarly, Tongay *et al.*[120] analysed monolayers of MoS_2 and $MoSe_2$ through AFM images.

Applications

Mo–chalcogenide nanostructured materials offer great scope in modern technological advancement. They are suitable for a variety of electronic and optoelectronic applications due to tailoring of their band gap and nature of the structure, *e.g.* simple spherical nanoparticles to layered structures can alter the properties, leading to possibilities of new applications. Not only pure MoX_2 nanostructured materials but their hybrid counterparts add tremendous value in converting traditional applications to modern requirements. In search of hybrid materials, researchers tried to combine nanoparticles with graphene for betterment of electrical and thermal properties. Indeed, it has been reported that graphene, having excellent conductivity when combined with MoX_2, may get further enriched, opening new avenues in the field of catalysis. In addition, MoX_2 can tackle the no bandgap problem of graphene. Therefore, the fabrication of hybrid structures achieving a synergistic effect is the latest research trend. Several reports and reviews were published discussing various applications of Mo–chalcogenides and a few of them are referred in this article.[168,169]

Mo–dichalcogenides have been proposed as potential materials for energy applications such as thermoelectrics,[170] Li/Na-ion batteries,[10] supercapacitors,[11] *etc.* Due to the high ionic conductivity and surface area, they are potential materials for electrical double layers in supercapacitors.[171] Hydrothermally synthesized $MoSe_2$ has shown a specific capacitance of 133 F g^{-1} at a current density of 2 A g^{-1} in a full solid-state supercapacitor, thereby opening avenues for flexible supercapacitors.[172]

Table 2 presents some of the important applications of MoX_2 compounds prepared by various methods. The following sections discuss some selected applications of layered molybdenum dichalcogenide compounds in their intrinsic forms and integrated with other materials wherever seems appropriate.

Catalysis

Electrocatalysis. The world is pursuing renewable and clean sources of energy. Molecular hydrogen is by far the cleanest fuel. Given the right catalyst, the hydrogen evolution reaction (HER) is the most efficient and simplest electrode reaction to produce hydrogen. Production of hydrogen *via* splitting of water through the HER is a $2e^-$ electrochemical reaction and is believed to be an excellent way to produce renewable hydrogen fuel. In the HER, the H^+ ions from the solution combine with electrons on the surface of the catalyst to produce H_2 gas. Therefore, adsorption and binding of hydrogen becomes the most essential step. This step is quantized in the form of Gibbs free energy of adsorption (ΔG_H). The lower the ΔG_H value, the higher the binding efficiency. The layered nature of MoX_2 compounds makes them highly suitable for catalysis due to the presence of dangling bonds and exposed edges,[7,173] whereas basal planes are catalytically inert. Therefore, nanosized MoX_2 are more active due to increased accessible edges as compared to their bulk counterparts due to the increased surface area.

HER devices use acidic electrolytes, and hence MoS_2 and $MoSe_2$ act as acid-resistant catalysts.[174] Several reports have reported the remarkable capability of MoX_2 compounds in the HER. In HER electrocatalysis, the HER catalyst should minimize the overpotential and should have a low Tafel slope (intrinsic properties of the catalyst) and consequently increase the process efficiency. It is therefore warranted that researchers should undertake advanced research to develop highly active HER catalysts including materials that are highly abundant and inexpensive. The HER on a commercial Pt surface gives a Tafel slope of $\sim$ 30 mV dec^{-1}, while commercial MoS_2 shows a value of $\sim$115 mV dec^{-1}. MoS_2 has the advantages of being resistant to sulphur poisoning and highly reactive. Xu *et al.*[110] explored MoS_2 QDs and nanosheets for HER performance. The QDs gave an overpotential of about 350 mV, whereas the mixture gave an overpotential of 120 mV which was due to the high number of active edges in interspersed QDs and nanosheets and obtained a Tafel slope of $\sim$69 mV dec^{-1}. There was a negligible change in performance even after the 2000th cycle. The main focus is to maximize exposed sites to obtain a higher efficiency. For this motive, MoS_2 has been supported on various materials like Au, graphene, CdS, ZnS, carbon fibres, SiO_2, *etc.* MoS_2/RGO hybrids synthesized by Yanguang Li and co-workers[60] gave a very low

overpotential and a small Tafel slope. They obtained a Tafel slope of ~41 mV dec^{-1} from MoS_2/RGO hybrids. This catalyst was reported to be highly durable and reproducible even after 1000 cycles. The progress in MoS_2 based HER performance was thoroughly reviewed by He *et al.*[175]

On the other hand, $MoSe_2$ show HER performance with a much lower Tafel slope and a lower overpotential than MoS_2 as $MoSe_2$ provides a higher coverage area for hydrogen adsorption.[52] Guo *et al.*[176] fabricated a nanocomposite of $MoSe_2$/RGO and found that the electrocatalytic activity was well comparable to that of the commercial Pt/C material. The role of electrical conductivity is very pivotal for HER performance. The electrical conductivity of 1T-MoX_2 is much higher than that of 2H-MoX_2. Using 1T-MoX_2 provides more active sites and a greater electrical conductivity leading to an enhancement in HER activity.[177–179] Zhang *et al.*[180] reported core–shell type 1T@2H-$MoSe_2$ nanosheets *via* a simple hydrothermal method with excellent HER performance having a Tafel slope of 41 mV dec^{-1} equal to that reported for MoS_2 and an overpotential of 20 mV.[60] Huang *et al.*[181] synthesized $MoSe_2/SnO_2$ composites where $MoSe_2$ nanosheets were decorated on SnO_2 nanotubes. This open structure made the edges fully accessible leading to high HER activity with a Tafel slope of 51 mV dec^{-1}. These reports suggest that a secondary material is required in order to expose the edges and make full utilisation of these MoX_2 compounds. Similarly, Singh *et al.*[182] reported the improved performance of the $MoSe_2$/SnS nanocomposite for water splitting.

When it comes to tellurium-based Mo nanostructures, 2H-$MoTe_2$ was found to be catalytically inert; however, 1T-$MoTe_2$ was found to be a competent electrocatalyst for the HER with a moderate current density of −10 mA cm^{-2} at about 360 mV in sulfuric acid.[183,184] Likewise, Qiao *et al.*[185] reported liquid exfoliated $MoTe_2$ nanosheets for electrocatalytic activity showing a Tafel slope of 118.9 mV dec^{-1} with an overpotential of 309 mV. As the HER activity is extensively dependent on the exposed edges, a large portion of the layered surface, *i.e.*, the basal plane, remains useless. By activating the basal planes of 1T′-$MoTe_2$, McGlynn *et al.*[28] reported an improvement of overpotential in $MoTe_2$ from 320 to 178 mV with the Tafel slope increasing to 116 mV dec^{-1} from 68 mV dec^{-1}. This value was obtained by applying a reverse bias to the $MoTe_2$ electrodes which introduced extra electrons leading to activation of basal planes resulting in superior HER activity. There is truly little research carried out for HER applications of $MoTe_2$ and it may be possible to further enhance its applicability by combining it with other materials. In view of this, Donglin Lu and co-workers[186] synthesized 1T′-$MoTe_2$ on a carbon cloth substrate *via* the CVD process. The activity of the material was evident from the Tafel slope value of 127 mV dec^{-1} and the overpotential value of −230.7 mV. The inter-combination of MoX_2 may further enhance their activity, but no reports on that matter can be found. Hence, this area can be looked upon to expand their application and gain more insights into their properties.

Photocatalysis. MoS_2, being chemically inert, easily available, and having low toxicity, good thermal stability and high absorption capacity, has been considered as a useful heterogenous photocatalyst for dye degradation and water decontamination through advanced oxidation processes (Fig. 24). The small bandgap of TMDs, especially those of MoS_2 and $MoSe_2$, allows solar energy to be harvested in the visible region for photocatalytic degradation of organic pollutants. The narrow bandgap of nano-$MoSe_2$ (~1.55 eV) is highly resistant to photocorrosion. The photocatalytic activity of $MoSe_2$ is limited by virtue of a higher charge carrier recombination rate, poor visible light adsorption and a low electrical conductivity. These drawbacks can be overcome by the synergistic effect of other nanomaterials. Many reports mention the use of TMD composites with other materials like ZnO, TiO_2, GO, and rGO as photocatalysts.[187] The review article by Wu *et al.*[188] gives a general comparison of the photocatalytic efficiency of MoS_2 in combination with such materials. Ritika *et al.*[18] observed more than 95% degradation of 10 ppm methylene blue (MB) solution in 20 minutes using a meager quantity (0.15 g l^{-1}) of the MoS_2–ZnO catalyst. However, the degradation percentage was found to be pH dependent with maximum degradation observed at pH 11. According to them, the combination of MoS_2 and ZnO has reduced the recombination rate of charge carriers due to fast charge transfer in the conduction bands of MoS_2 and ZnO leading to a high rate of reaction. Wu *et al.*[189] synthesized $MoSe_2$ composites with reduced graphene oxide (rGO) so as to minimize the recombination rate and increase the charge transfer. The hydrothermal method resulted in formation of 2–3 layer thick $MoSe_2$ nanosheets vertically aligned on the surface of rGO. These nanocomposites were able to remove more than 90% of MB and RhB effluents. Haipengchu *et al.*[50] reported up to 90% reduction of Cr(VI) in visible light in 2 h with $MoSe_2/TiO_2$ nanocomposites. They also compared the results with those of individual $MoSe_2$ and TiO_2 which resulted in a much lower reduction of the same up to 60% and 5% only. The maximum efficiency was obtained when the ratio of $MoSe_2$ and TiO_2 was 2 : 1 and further increase in the amount of TiO_2 decreased the reduction efficiency. Mittal *et al.*[190] studied the photocatalytic activity of $MoSe_2$ and polyaniline (PANI) nanocomposites. These composites were effective against both

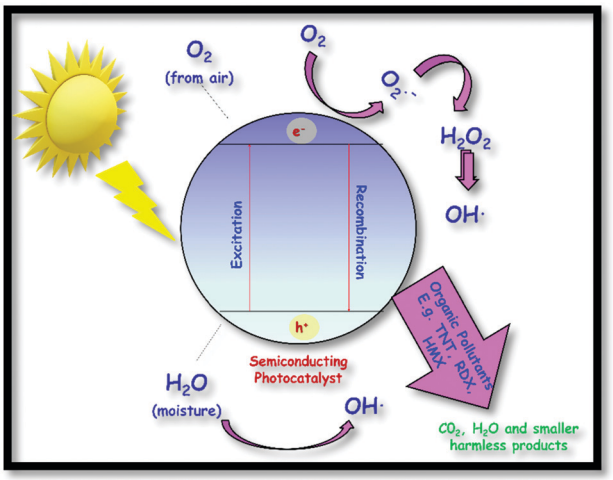

Fig. 24 Typical photodegradation mechanism *via* advanced oxidation processes (AOPs).

cationic and anionic dyes due to the presence of both +ve and −ve charges on the surface and thus 80% degradation was observed for Congo red (CR) and Rhodamine B (RhB) by a $MoSe_2$/PANI composite with a 2 : 1 ratio.

Huang *et al.*[191] were even successful in degrading nitro aromatic compound contaminants present in water with the help of the as-synthesized $MoSe_2$ microspheres composed of $MoSe_2$ nanosheets. However, in the case of Mo-tellurides, out of two phases of $MoTe_2$, only the 2H phase has fairly good photoresponsivity to visible and infrared light.[192]

Water desalination and decontamination

Shortage of clean potable water is the major problem faced by most of the population. It is realized by the researchers that, without disturbing natural hydrological cycles, seawater desalination technologies are the best alternative to the problem of water shortage. Driven by their huge ecological benefits, they are gaining a lot of research interest. MoS_2 nanosheets are highly effective in decontaminating water by absorbing heavy ions. The monolayer nanosheets have a high absorption capacity due to a high surface area and excellent affinity towards many transition metal ions (heavy metals) such as Hg^{2+}, Ag^{+}, Pb^{2+}, Zn^{2+}, and Cd^{2+} (soft Lewis acids) due to the presence of S^{2-} ions (soft Lewis base) on the exposed edges. The order of selectivity is $Hg^{2+} > Pb^{2+} > Zn^{2+} > Cd^{2+}$ according to the order of their softness. These negatively charged ions are also helpful in dispersing these nanomaterials into water. The H^{+} or other intercalating ions such as Li^{+} are present in contaminated water as counterions with a negative charge on the surface. These ions are replaced by the contaminant metal ions and make complexes with sulfur ions, leading to decontamination of water. Another factor in the adsorption of these ions on the nanosheets is that the ions in the water are pulled and hold together by the surface ions through electrostatic force of attraction. Thus, the whole process is believed to be based on the interaction at the surface as well as the inner layer complex formation.[193] Therefore, the best adsorbent for decontamination would be the one with a higher sulphur content, large surface area and high pore volume having enough size to accommodate the ions. Kankeu *et al.*[194] recently synthesized MWCNT/MoS_2 hybrids loaded with mercaptopropyl trimethoxysilane to create a sulfur rich surface and then tested them for removing mercury ions from water. A high absorption capacity of 0.9661 mg g^{-1} was achieved, and the study also revealed that the decontamination takes place through the chemisorption phenomenon. Ai *et al.*[195] reported the absorption capacity of the hydrothermally prepared MoS_2 nanosheets as high as 2563 mg g^{-1} and excellent mercury selectivity. The concentration of mercury ions was drastically reduced from 10 000 ppb to 0.3 ppb by using 10 mg of the adsorbent for 100 mL solution. MoS_2 adsorbents are also highly efficient in absorbing cationic/alkaline dyes like MB, malachite green (MG), and RhB[196] through van der Waals forces and electrostatic forces of attraction. Massey *et al.*[197] in their study found that 0.1 g of the synthesized MoS_2 nanosheets were able to adsorb 90% of MB within 10 minutes from its >100 ppm solution and has shown good recyclability. Similarly, an 80% removal efficiency was observed in the case of MG and RhB within an hour. However, acidic dyes like CR and fuchsin acid have shown very low adsorption. In contrast to most studies, fungus like MoS_2 nanosheets, hydrothermally prepared by Song *et al.*,[198] were selective towards Congo red instead of MB or RhB. MoS_2 nanosheets with a contact angle greater than 80° (against water) exhibit hydrophobicity and hence can be helpful in removal of oils from water.[199] These nanostructures having high adsorption properties combined with photocatalytic properties serve as productive and cost-efficient materials for water purification. A review article discussing specifically the adsorption of heavy metal ions in water on MoS_2 has been recently published. It thoroughly explains the mechanism involved, the factors affecting the adsorption process and its efficiency compared to other adsorbents.[200] In their study, Hieranian *et al.*[201] applied membrane technology for the desalination of water. As it is obvious that the thinner the membrane, the greater the water flux through it, single layer MoS_2 nanosheets with nanopores were applied, achieving a desalination capacity up to 80%.

Sensors

The use of nanocrystalline MoX_2 as a sensing material is widely being studied. The most reported MoX_2 based sensors are field effect transistor (FET) type. The advantage of MoS_2 in FETs has been thoroughly reviewed by Singh *et al.*[202] The general device structure of a FET with the example of MoS_2 as the sensing material is depicted in Fig. 25.[203] The strength of MoX_2 transistors lies in a large bandgap, which offers a high on/off ratio, and the layered nature provides excellent electrostatic integrity. Therefore, they can overcome the limitations in graphene-based devices due to the absence of bandgap despite having an excellent mobility of up to 2×10^5 cm^2 V^{-1} s^{-1}.[204] They may not be ideal candidates for high performance applications but they can be conveniently utilized for applications having low-power requirements. MoS_2-based FET sensors have exhibited exceptional charge carrier mobilities and high on/off ratios with great sensitivity in the detection of biomolecules, heavy metal ions, and toxic gases.[193] The following sub-sections discuss the use of molybdenum dichalcogenides in gas sensors, photo-detectors and bio-sensors.

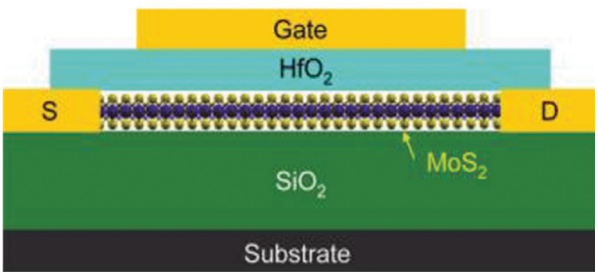

Fig. 25 Representation of the device structure of a MoS_2 transistor. Reprinted with permission from ref. 203 [Y. Yoon, K. Ganapathi and S. Salahuddin, *Nano Lett.*, 2011, **11**, 3768–3773]. Copyright 2011 American Chemical Society.

Gas sensors

Gaseous toxicity detection is an essential requirement for human and environmental health. The timely monitoring and understanding of effluents from industries and the environment is a burning issue for living organisms. In this regard, the development of 2D sensors which can work at room temperature has become important. Several reports endorsed nano-MoS_2 for gas-sensing applications due to the ample surface area and abundant surface-active sites. Yoon *et al.*[203] reported a 0.5 to 320 $cm^2\ V^{-1}\ s^{-1}$ variation in field effect mobility values with an on/off $>10^{10}$ order of magnitude when sensing was performed using a thin MoS_2 FET. MoS_2-based FET devices are useful in the detection of various gases (*e.g.*, H_2, NH_3, and NO_2).[13,205] As the 2D configuration allows better adsorption of gas molecules, most reports use MoS_2 nanosheets for gas detection.[206] Li *et al.*[207] detected NO gas up to the conc. of 0.8 ppm through a mechanically exfoliated MoS_2 nanosheet based FET and also observed that multilayer MoS_2 was more efficient than the monolayer analogue. It is reported that the resistance increases due to the absorption of electron-withdrawing NO on MoS_2.[208] Late *et al.*[26] reported a room temperature $MoSe_2$ sensor for the detection of NH_3 up to a level of 50 ppm. The detection of hazardous NO_2 and NH_3 gases up to a level of 1 ppm was reported using a $MoSe_2$ based FET sensor[209] and up to a level of 20 ppb for exfoliated MoS_2.[210] It is often realized that MoX_2 nanomaterials offer high sensitivity, but the recovery time is longer when compared to metal oxides.[211,212]

Photo-detectors

Atomically thin MoS_2 shows excellent sensing towards chemicals and gaseous molecules and is also a very good photosensor owing to its sensitivity to the external environment and illumination conditions. Late *et al.*[12] synthesized monolayer MoS_2 FETs and studied the origin of hysteresis in these devices. They stated that the main cause of hysteresis was the absorption of water molecules which induce trap states in the material. The authors also mentioned that with MoS_2 being highly photosensitive, white light illumination can significantly contribute to hysteresis. It was thereby suggested that the controlled hysterical behaviour of FETs can be utilized in humidity sensors and the photosensitive behaviour can be utilised in photo-detectors.[213] Li *et al.*[116] fabricated phototransistors using 1L MoS_2 and SiO_2 as dielectric layers which have shown a photo-responsivity of 7.5 mA W^{-1} at an applied voltage of nearly 50 V. Similarly, phototransistors fabricated from 1L to 3L MoS_2 exhibited a photo-responsivity of nearly 100 mA W^{-1} at an applied voltage of up to 10 V. The report has also shown that 1L and 2L MoS_2 detected green light and 3L nanosheets were responsive to red light.[214] Lopez-Sanchez *et al.*[215] fabricated 1L-MoS_2 phototransistors and reported an excellent photoresponsivity of 880 A W^{-1}. Hang *et al.*[121] fabricated phototransistors based on 3L $MoSe_2$, demonstrating an on/off ratio of $\sim 10^5$ and a carrier mobility of 1.79 $cm^2\ V^{-1}\ s^{-1}$. The humidity sensors developed from $MoSe_2$ nanoflowers showed a sensitivity of more than 70% with response and recovery times of 53 seconds and 13 seconds, respectively.[14] Selamneni *et al.*[216] fabricated a near infrared (NIR) photodetector incorporating $MoSe_2$ nanoflowers onto cellulose paper and reported a photoresponsivity of 9.73 mA W^{-1} when illuminated by 780 nm light and the expected improvement with an enhancement in light intensity. The fabricated device was flexible and robust in nature, promising its future in nanoelectronics. Having a narrower bandgap than nano-MoS_2 and $MoSe_2$, nano-$MoTe_2$ is a favourable candidate for NIR photodetectors. The use of thin layered $MoTe_2$ is very prominent in FETs.[129,217] Few-layer $MoTe_2$ has the least direct bandgap in the MoX_2 family and therefore can be operated in the visible to infrared energy range. Giri *et al.*[218] reported 3L $MoTe_2$ photodetectors showing photoresponsivities over the range of 300 to 1100 nm with a maximum photoresponsivity of $\sim$53.1 mA W^{-1} at 870 nm and a minimum value of 30 mA W^{-1} at 1100 nm. By introducing an electron tunnelling mechanism, interestingly, Yin *et al.*[124] reported an outstanding photoresponsivity of 2560 A W^{-1} and an electron mobility of 25.2 $cm^2\ V^{-1}\ s^{-1}$ using few-layered $MoTe_2$ as the channel in a transistor.

Bio-sensors

Owing to their excellent electrochemical and luminescence properties, MoS_2-based nanomaterials have been endorsed as excellent biosensing probes for the analyte detection over a wide range.[219] Due to their luminescence quenching properties and multidimensional structures, such chalcogenides can cover a wide band of applications.[193] Indeed, there are several reports that document successful utilization of MoS_2 nanosheets in the detection of biomolecules and metal ion contaminants.[220,221] MoS_2 nanostructures are highly biocompatible up to a conc. of 100 ppm,[222] and thus it facilitates the monitoring of Ag^+ ions in *E. coli* cells.[220] Other species such as proteins[223,224] and H_2O_2[225] have also been sensed using MoS_2 nanosheets. A strong photoluminescence is observed in nanocrystalline MoS_2 which is absent in the bulk form. This property renders it useful in bio-imaging probes. Additionally, TMDs have a superior ionic conductivity and electron mobility to the respective oxides.[226] Sha *et al.*[16] demonstrated detection of uric acid *via* fabrication of a flexible, highly sensitive and low-cost electrochemical sensor based on MoS_2 nanosheets. The review by Sha *et al.*[17] encompasses the biosensing applications of MoS_2, emphasizing its potential in biomedical and environmental detection in terms of sensitivity and selectivity.

Photovoltaics

Because of their high electron mobility and radiation absorption properties, MoX_2 compounds have been widely explored for solar cells. It is therefore expected and has also been demonstrated that MoS_2 can overtake Si as the absorber layer because of its better absorption efficiency. It can be used as the charge transport layer as well as the buffer layer in solar cells. The recently published review article by Nawz *et al.*[227] highlights the potential of MoS_2 in solar cells. Dye sensitized solar

cells (DSSCs) use toxic ruthenium-based dyes which degrade at high temperatures and use expensive Pt electrodes. MoS_2, however, is highly stable and absorbs in the visible range and therefore has been widely applied; for example, Ortiz-Quelis *et al.*[9] studied MoS_2 as a photoanodic material in dye-sensitized solar cells, resulting in an increased photocurrent. A 6% conversion efficiency was reported using the MoS_2 counter electrode.[228] $MoSe_2$ and $MoTe_2$ and their composites can be good alternatives to Pt electrodes due to their good electrocatalytic activity.[229] Bi *et al.*[230] reported a conversion efficiency comparable to that of Pt electrodes in DSSCs using nitrogen doped graphene templated $MoSe_2$ hollow spheres. Hussain *et al.*[100] demonstrated a conversion efficiency of 7.25% using $MoTe_2$ as the counter electrode as compared to an 8.15% efficiency obtained using the commercial Pt electrode. An enhancement in the conversion efficiency, *i.e.*, 8.07%, was reported using $MoSe_2/MoTe_2$.[231] It was also shown that, with an increase in film thickness, the efficiency decreased. MoS_2 has also been used in organic solar cells (OSCs) as it has been reported to be capable of absorbing 5–10% more incident light as compared to GaAs and Si.[232] Similarly, using $MoSe_2$ QDs in OSCs, Lian *et al.*[233] achieved a high conversion efficiency of 17%. $MoSe_2$ has also marked its role in copper indium gallium selenide (CIGS) solar cells where the selenization process results in formation of a $MoSe_2$ interlayer between the Mo layer (back contact) and the absorber layer. This thin $MoSe_2$ layer has been reported to reduce the Schottky barrier height.[234] The deposition techniques, doping concentration and thickness greatly influence the performance of CIGS solar cells.[235]

Biology

Mo dichalcogenides have recently become useful materials for cancer cell detection and understanding their interaction provides useful information for biologists. The advancement in nanotechnology and bioscience is thus desired to undertake such newer materials for better diagnostics as well as sensing and bio-imaging technologies. There are, however, only a few reports on this topic. It is often desired that spherical particles of semiconductors, especially those with light emitting properties or generally photonic properties, can be exploited for biological applications as their optical behaviour will possibly alter to provide useful information. Appropriately, Xu *et al.*[110] tested the cytotoxicity of MoS_2 quantum dots (QDs) prepared by a simple sonochemical method against HeLa and HEK293T cells and found them to be less toxic, indicating that such particles are safer to cells for obtaining useful information. These QDs also show excellent fluorescence in the biological environment, permeable in the cell membrane but not in the nuclei promising non-toxic and bio-compatible probes for *in vitro* imaging. When compared with other TMD materials which stay accumulated in the organs, PEG-coated MoS_2 nanosheets have shown faster degradation and removal from the body within a month.[236] MoS_2 oxidation products readily undergo degradation and release soluble Mo-compounds and hence are responsible for the biocompatible nature of MoS_2.[237]

Conclusions

This survey has revealed that nanostructured molybdenum dichalcogenides are a hot area of research currently. Research in this area is still in its infancy and there is a lot more to touch upon in terms of convenient synthesis methods, insights into the structure and morphology, and also their potential in various energy storage and conversion applications. In an increasingly competitive material fabrication market, eco-friendly and reusable materials are the core needs of advanced technology at a reasonable cost. The research output of MoX_2 type compounds could lead to the development of better lubricants and tribological, model, advanced, multifunctional and smart materials. This trend will foster cutting-edge tech innovations in the materials space and provide invaluable insights into various aspects of material fabrication. In this article, synthesis of nanocrystalline MoX_2 (X = S, Se, Te) by various methods such as hydrothermal, solvothermal, thermal, chemical vapour deposition, microwave, sonochemical, mechanical and chemical exfoliation, and pulsed laser ablation routes was discussed thoroughly. Analysis and characterization are the key requirements for a synthetic chemist, and therefore a special focus was given to the various techniques that are used in the analysis of these structurally unique semiconductors. It is expected that this review will give a good overview of the state of the art to entry level researchers in this field and the quest for simpler synthesis methods for the synthesis of this type of compound on the laboratory scale will continue. Hence, unique types of morphologies will emerge which may give rise to unique properties. The article will encourage researchers to look beyond MoS_2 and $MoSe_2$ and also look into the potential of $MoTe_2$ which is a unique material as it can also be grown in both 2H and 1T′ forms with a possibility of tuning the phases as desired for a variety of promising yet challenging electronic applications. Polymorphism control of $MoTe_2$ is scientifically interesting and requires more comprehensive investigations. An overview of the past progress and recent research revealed that there is a spectrum of interest stretching from the considerably basic to the very applied. It has been revealed in this article that TMDs are excellent materials for a large number of applications but their potential can be further tuned and enhanced by integrating them with other inorganic or organic semiconducting materials. Thus, hybrid semiconductors with MoX_2 can augment their usefulness in a variety of applications such as gas sensors, FETs, water-desalination and decontamination, tailor-made electrocatalysis and photocatalysis, and biological applications remain to be studied.

Author contributions

Priyanka and P. K. Khanna visualized the entire concept and drafted the original manuscript. H. G. Rubahn and Y. K. Mishra contributed in terms of value addition, and reviewed and edited the manuscript.

Conflicts of interest

There are no conflicts to declare.

Acknowledgements

DIAT authors thank the SPARC programme of the Govt of India (Grant No. SPARC/2018-2019/P573/SL) and Vice-chancellor DIAT (DU) for support and permission. The authors thank Dr BHS Thimappa for critical suggestions during the drafting of this article. Priyanka thanks Neha Bisht for useful suggestions.

SDU authors acknowledge the funding by Interreg Deutschland–Denmark with money from the European Regional Development Fund, project number 096-1.1-18 (Access and Acceleration), and from the ESS lighthouse on hard materials in 3D, SOLID, funded by the Danish Agency for Science and Higher Education, grant number 8144-00002B.

References

1 R. Sha, N. Vishnu and S. Badhulika, *Microchim. Acta*, 2018, **185**, 399.
2 R. Sha, A. Gopalakrishnan, K. V. Sreenivasulu, V. V. S. S. Srikanth and S. Badhulika, *J. Alloys Compd.*, 2019, **794**, 26–34.
3 J. Deepika, R. Sha and S. Badhulika, *Microchim. Acta*, 2019, **186**, 480.
4 R. Sha, A. Kadu, K. Matsumoto, S. Uno and S. Badhulika, *Eng. Res. Express*, 2020, **2**, 025020.
5 J. Huang, H. Liu, B. Jin, M. Liu, Q. Zhang, L. Luo, S. Chu, S. Chu and R. Peng, *Nanotechnology*, 2017, **28**, 275704.
6 S. Kou, X. Guo, X. Xu and J. Yang, *Catal. Commun.*, 2018, **106**, 60–63.
7 D. Kong, H. Wang, J. J. Cha, M. Pasta, K. J. Koski, J. Yao and Y. Cui, *Nano Lett.*, 2013, **13**, 1341–1347.
8 P. Li, K. Yuan, D.-Y. Lin, X. Xu, Y. Wang, Y. Wan, H. Yu, K. Zhang, Y. Ye and L. Dai, *Nanoscale*, 2017, **9**, 18175–18179.
9 E. O. Ortiz-Quiles and C. R. Cabrera, *FlatChem*, 2017, **2**, 1–7.
10 U. Krishnan, M. Kaur, K. Singh, M. Kumar and A. Kumar, *Superlattices Microstruct.*, 2019, **128**, 274–297.
11 R. Sha, P. C. Maity, U. Rajaji, T.-Y. Liu and T. K. Bhattacharyya, *J. Electrochem. Soc.*, 2022, **169**, 013503.
12 D. J. Late, B. Liu, H. S. Matte, V. P. Dravid and C. N. Rao, *ACS Nano*, 2012, **6**, 5635–5641.
13 D. J. Late, Y. K. Huang, B. Liu, J. Acharya, S. N. Shirodkar, J. Luo, A. Yang, D. Charles, U. V. Waghmare, V. P. Dravid and C. N. R. Rao, *ACS Nano*, 2013, **7**, 4879–4891.
14 N. T. Shelke and D. J. Late, *Sens. Actuators, A*, 2019, **295**, 160–168.
15 S. Barua, H. S. Dutta, S. Gogoi, R. Devi and R. Khan, *ACS Appl. Nano Mater.*, 2017, **1**, 2–25.
16 R. Sha, N. Vishnu and S. Badhulika, *Sens. Actuators, B*, 2019, **279**, 53–60.
17 R. Sha and T. K. Bhattacharyya, *Electrochim. Acta*, 2020, **349**, 136370.
18 Ritika, M. Kaur, A. Umar, S. K. Mehta, S. Singh, S. K. Kansal, H. Fouad and O. Y. Alothman, *Materials*, 2018, **11**(11), 2254.
19 W. Li, Y. Yang, J. K. Weber, G. Zhang and R. Zhou, *ACS Nano*, 2016, **10**, 1829–1835.
20 W. Hirunpinyopas, E. Prestat, S. D. Worrall, S. J. Haigh, R. A. W. Dryfe and M. A. Bissett, *ACS Nano*, 2017, **11**, 11082–11090.
21 H. Wu, R. Yang, B. Song, Q. Han, J. Li, Y. Zhang, Y. Fang, R. Tenne and C. Wang, *ACS Nano*, 2011, **5**, 1276–1281.
22 J. A. Wilson and A. D. Yoffe, *Adv. Phys.*, 1969, **18**, 193–335.
23 Y. Yu, G. H. Nam, Q. He, X. J. Wu, K. Zhang, Z. Yang, J. Chen, Q. Ma, M. Zhao, Z. Liu, F. R. Ran, X. Wang, H. Li, X. Huang, B. Li, Q. Xiong, Q. Zhang, Z. Liu, L. Gu, Y. Du, W. Huang and H. Zhang, *Nat. Chem.*, 2018, **10**, 638–643.
24 A. Kuc, *Chemical Modelling: Volume 11*, The Royal Society of Chemistry, 2015, vol. 11, pp. 1–29.
25 C. Guo, J. Pan, H. Li, T. Lin, P. Liu, C. Song, D. Wang, G. Mu, X. Lai, H. Zhang, W. Zhou, M. Chen and F. Huang, *J. Mater. Chem. C*, 2017, **5**, 10855–10860.
26 D. J. Late, T. Doneux and M. Bougouma, *Appl. Phys. Lett.*, 2014, **105**, 233103.
27 S. Tongay, J. Zhou, C. Ataca, K. Lo, T. S. Matthews, J. Li, J. C. Grossman and J. Wu, *Nano Lett.*, 2012, **12**, 5576–5580.
28 J. C. McGlynn, T. Dankwort, L. Kienle, N. A. G. Bandeira, J. P. Fraser, E. K. Gibson, I. Cascallana-Matias, K. Kamaras, M. D. Symes, H. N. Miras and A. Y. Ganin, *Nat. Commun.*, 2019, **10**, 4916.
29 J.-H. Huang, K.-Y. Deng, P. S. Liu, C.-T. Wu, C.-T. Chou, W.-H. Chang, Y.-J. Lee and T.-H. Hou, *Adv. Mater. Interfaces*, 2017, **4**, 1700157.
30 K. Ueno and K. Fukushima, *Appl. Phys. Express*, 2015, **8**, 095201.
31 J.-H. Huang, K.-Y. Deng, P.-S. Liu, C.-T. Wu, C.-T. Chou, W.-H. Chang, Y.-J. Lee and T.-H. Hou, *Adv. Mater. Interfaces*, 2017, **4**, 1700157.
32 C. Ruppert, O. B. Aslan and T. F. Heinz, *Nano Lett.*, 2014, **14**, 6231–6236.
33 K. K. Kam and B. A. Parkinson, *J. Phys. Chem.*, 1982, **86**, 463–467.
34 K. F. Mak, C. Lee, J. Hone, J. Shan and T. F. Heinz, *Phys. Rev. Lett.*, 2010, **105**, 136805.
35 W. S. Yun, S. W. Han, S. C. Hong, I. G. Kim and J. D. Lee, *Phys. Rev. B: Condens. Matter Mater. Phys.*, 2012, **85**(3), 033305.
36 H. Liu, K. K. A. Antwi, S. Chua and D. Chi, *Nanoscale*, 2014, **6**, 624–629.
37 J. Mann, Q. Ma, P. M. Odenthal, M. Isarraraz, D. Le, E. Preciado, D. Barroso, K. Yamaguchi, G. von Son Palacio, A. Nguyen, T. Tran, M. Wurch, A. Nguyen, V. Klee, S. Bobek, D. Sun, T. F. Heinz, T. S. Rahman, R. Kawakami and L. Bartels, *Adv. Mater.*, 2014, **26**, 1399–1404.
38 Q. Feng, Y. Zhu, J. Hong, M. Zhang, W. Duan, N. Mao, J. Wu, H. Xu, F. Dong, F. Lin, C. Jin, C. Wang, J. Zhang and L. Xie, *Adv. Mater.*, 2014, **26**, 2648–2653.
39 M. Chhowalla, D. Voiry, J. Yang, H. S. Shin and K. P. Loh, *MRS Bull.*, 2015, **40**, 585–591.
40 W. J. Li, E. W. Shi, J. M. Ko, Z. z Chen, H. Ogino and T. Fukuda, *J. Cryst. Growth*, 2003, **250**, 418–422.

41 S. V. P. Vattikuti and C. Byon, *J. Nanomater.*, 2015, **2015**, 1–11.
42 Y. Tian, Y. He and Y. Zhu, *Chem. Lett.*, 2003, **32**, 768–769.
43 G. Nagaraju, C. Tharamani, G. Chandrappa and J. Livage, *Nanoscale Res. Lett.*, 2007, **2**, 461–468.
44 B. Pourabbas and B. Jamshidi, *Chem. Eng. J.*, 2008, **138**, 55–62.
45 M. Manuja, V. Sarath Krishnan and G. Jose, *IOP Conf. Ser.: Mater. Sci. Eng.*, 2018, **360**, 012015.
46 S. X. Hou, C. Wu and Y. J. Huo, *Ceram.-Silik.*, 2017, **61**(2), 158–162.
47 V. Barough, E. S. Iranizad, A. Bayat and K. Hemmati, *J. Electroanal. Chem.*, 2018, **823**, 278–286.
48 Y. Yan, B. Sun and D. Ma, *Chem. Phys. Lett.*, 2015, **638**, 103–107.
49 B. Mao, T. Bao, J. Yu, L. Zheng, J. Qin, W. Yin and M. Cao, *Nano Res.*, 2017, **10**, 2667–2682.
50 H. Chu, X. Liu, B. Liu, G. Zhu, W. Lei, H. Du, J. Liu, J. Li, C. Li and C. Sun, *Sci. Rep.*, 2016, **6**, 35304.
51 Y. Peng, Z. Meng, C. Zhong, J. Lu, W. Yu, Y. Jia and Y. Qian, *Chem. Lett.*, 2001, 772–773.
52 H. Tang, K. Dou, C.-C. Kaun, Q. Kuang and S. Yang, *J. Mater. Chem. A*, 2014, **2**, 360–364.
53 H. Mittal and M. Khanuja, *Environ. Sci. Pollut. Res. Int.*, 2020, **27**(19), 23477–23489.
54 W. Xiao, D. Bukhvalov, Z. Zou, L. Zhang, Z. Lin and X. Yang, *ChemSusChem*, 2019, **12**, 5015–5022.
55 V. Ghritlahre, J. Kumari and P. Agarwal, *AIP Conf. Proc.*, 2018, **1953**, 050048.
56 S. Setayeshgar, M. Karimipour, M. Molaei, M. R. Moghadam and S. Khazraei, *Int. J. Hydrogen Energy*, 2020, **45**, 6090–6101.
57 G. Liu, S. Dai, P. Li, B. Zhu, Z. Wu and Y. Gu, *Opt. Mater.*, 2019, **95**, 109240.
58 H. Li, S. Gu, Z. Sun, F. Guo, Y. Xie, B. Tao, X. He, W. Zhang and H. Chang, *J. Mater. Chem. A*, 2020, **8**(26), 13038–13048.
59 J. H. Zhan, Z. D. Zhang, X. F. Qian, C. Wang, Y. Xie and Y. T. Qian, *J. Solid State Chem.*, 1998, **141**, 270–273.
60 Y. Li, H. Wang, L. Xie, Y. Liang, G. Hong and H. Dai, *J. Am. Chem. Soc.*, 2011, **133**, 7296–7299.
61 B. Zhu, B. Lin, Y. Zhou, P. Sun, Q. Yao, Y. Chen and B. Gao, *J. Mater. Chem. A*, 2014, **2**, 3819–3827.
62 Y. Sun, S. Wang and Q. Wang, *Front. Chem. China*, 2009, **4**, 173–176.
63 J. Wu, B. Li, Y. Shao, X. Wu and Y. Sun, *J. Mater. Sci.*, 2020, **55**, 2129–2138.
64 Q. Jiang, Y. Lu, Z. Huang and J. Hu, *Appl. Surf. Sci.*, 2017, **402**, 277–285.
65 D. Duphil, S. Bastide and C. Lévy-Clément, *J. Mater. Chem.*, 2002, **12**, 2430–2432.
66 J. C. Park and H. Song, *Chem. Mater.*, 2007, **19**, 2706–2708.
67 D. Sun, S. Feng, M. Terrones and R. E. Schaak, *Chem. Mater.*, 2015, **27**, 3167–3175.
68 Y. Wang, F. Zhang, Q. Wang, P. Yang, H. Lin and F. Qu, *Nanoscale*, 2018, **10**, 14534–14545.
69 C. Zhang, X. Chen, Z. Peng, X. Fu, L. Lian, W. Luo, J. Zhang, H. Li, Y. Wang and D. Zhang, *CrystEngComm*, 2018, **20**, 2491–2498.
70 W. Guo, Y. Chen, L. Wang, J. Xu, D. Zeng and D.-L. Peng, *Electrochim. Acta*, 2017, **231**, 69–76.
71 J. M. Huang and D. F. Kelley, *Chem. Mater.*, 2000, **12**, 2825–2828.
72 X. Geng, Y. Yu, X. Zhou, C. Wang, K. Xu, Y. Zhang, C. Wu, L. Wang, Y. Jiang and Q. Yang, *Nano Res.*, 2016, **9**, 2641–2651.
73 M. S. Hassan, A. Jana, S. Gahlawat, N. Bhandary, S. Bera, P. P. Ingole and S. Sapra, *Bull. Mater. Sci.*, 2019, **42**, 74.
74 Y. Sun, Y. Wang, D. Sun, B. R. Carvalho, C. G. Read, C. H. Lee, Z. Lin, K. Fujisawa, J. A. Robinson, V. H. Crespi, M. Terrones and R. E. Schaak, *Angew. Chem., Int. Ed.*, 2016, **55**, 2830–2834.
75 L. Qiu, Y. Wei, V. G. Pol and A. Gedanken, *Inorg. Chem.*, 2004, **43**, 6061–6066.
76 M. Liu, Z. Wang, J. Liu, G. Wei, J. Du, Y. Li, C. An and J. Zhang, *J. Mater. Chem. A*, 2017, **5**, 1035–1042.
77 Y. Feldman, G. L. Frey, M. Homyonfer, V. Lyakhovitskaya, L. Margulis, H. Cohen, G. Hodes, J. L. Hutchison and R. Tenne, *J. Am. Chem. Soc.*, 1996, **118**, 5362–5367.
78 N. K. Perkgoz and M. Bay, *Nano-Micro Lett.*, 2016, **8**, 70–79.
79 N. Kumar, R. Tomar, N. Wadehra, M. M. Devi, B. Prakash and S. Chakraverty, *Cryst. Res. Technol.*, 2018, **53**, 1800002.
80 S. Balendhran, J. Z. Ou, M. Bhaskaran, S. Sriram, S. Ippolito, Z. Vasic, E. Kats, S. Bhargava, S. Zhuiykov and K. Kalantar-Zadeh, *Nanoscale*, 2012, **4**, 461–466.
81 J. Jeon, J. Lee, G. Yoo, J. H. Park, G. Y. Yeom, Y. H. Jang and S. Lee, *Nanoscale*, 2016, **8**, 16995–17003.
82 X. L. Li and Y. D. Li, *Chem. – Eur. J.*, 2003, **9**, 2726–2731.
83 Y. Feldman, E. Wasserman, D. J. Srolovitz and R. Tenne, *Science*, 1995, **267**, 222–225.
84 M. Nath, A. Govindaraj and C. N. R. Rao, *Adv. Mater.*, 2001, **13**, 283–286.
85 V. M. A. Arreola, M. F. Salazar, T. Zhang, K. Wang, A. H. B. Aguilar, K. C. S. Reddy, E. Strupiechonski, M. Terrones and A. D. L. Bugallo, *2D Mater.*, 2021, **8**, 025033.
86 Y. H. Lee, X. Q. Zhang, W. Zhang, M. T. Chang, C. T. Lin, K. D. Chang, Y. C. Yu, J. T. Wang, C. S. Chang, L. J. Li and T. W. Lin, *Adv. Mater.*, 2012, **24**, 2320–2325.
87 F. Wypych and R. Schöllhorn, *J. Chem. Soc., Chem. Commun.*, 1992, **19**, 1386–1388.
88 W. Wang, H. Shu, D. Zhou, J. Wang and X. Chen, *Nanotechnology*, 2020, **31**, 335601.
89 N. Masurkar, N. K. Thangavel and L. M. R. Arava, *ACS Appl. Mater. Interfaces*, 2018, **10**, 27771–27779.
90 N. Liu, W. Choi, H. Kim, C. Jung, J. Kim, S. H. Choo, Y. Kwon, B. S. An, S. Hong, S. So, C. W. Yang, J. Hur and S. Kim, *Nanoscale*, 2020, **12**, 6991–6999.
91 D. S. Kong, H. T. Wang, J. J. Cha, M. Pasta, K. J. Koski, J. Yao and Y. Cui, *Nano Lett.*, 2013, **13**, 1341–1347.
92 J. C. Shaw, H. Zhou, Y. Chen, N. O. Weiss, Y. Liu, Y. Huang and X. Duan, *Nano Res.*, 2014, **7**, 511–517.
93 E. D. Hanson, L. M. Lilley, J. D. Cain, S. Hao, E. Palacios, K. Aydin, C. Wolverton, T. Meade and V. P. Dravid, *Mater. Chem. Phys.*, 2019, **225**, 219–226.

94 M. Nath and C. N. Rao, *Chem. Commun.*, 2001, 2236–2237.
95 D. Vikraman, S. Hussain, K. Akbar, K. Adaikalam, S. H. Lee, S.-H. Chun, J. Jung, H.-S. Kim and H. J. Park, *ACS Omega*, 2018, **3**, 5799–5807.
96 R. Beams, L. G. Cancado, S. Krylyuk, I. Kalish, B. Kalanyan, A. K. Singh, K. Choudhary, A. Bruma, P. M. Vora, F. Tavazza, A. V. Davydov and S. J. Stranick, *ACS Nano*, 2016, **10**, 9626–9636.
97 J. Lin, H. Wang and R. Y. Tay, *et al.*, *Nano Res.*, 2020, **13**, 2371–2377.
98 X. Xu, X. Li, K. Liu, J. Li, Q. Feng, L. Zhou, F. Cui, X. Liang, Z. Lei, Z. Liu and H. Xu, *Cryst. Growth Des.*, 2018, **18**, 2844–2850.
99 L. Zhou, K. Xu, A. Zubair, A. D. Liao, W. Fang, F. Ouyang, Y. H. Lee, K. Ueno, R. Saito, T. Palacios, J. Kong and M. S. Dresselhaus, *J. Am. Chem. Soc.*, 2015, **137**, 11892–11895.
100 S. Hussain, S. A. Patil, D. Vikraman, N. Mengal, H. Liu, W. Song, K. S. An, S. H. Jeong, H. S. Kim and J. Jung, *Sci. Rep.*, 2018, **8**, 29.
101 J. Zhou, F. Liu, J. Lin, X. Huang, J. Xia, B. Zhang, Q. Zeng, H. Wang, C. Zhu, L. Niu, X. Wang, W. Fu, P. Yu, T. R. Chang, C. H. Hsu, D. Wu, H. T. Jeng, Y. Huang, H. Lin, Z. Shen, C. Yang, L. Lu, K. Suenaga, W. Zhou, S. T. Pantelides, G. Liu and Z. Liu, *Adv. Mater.*, 2017, **29**, 1603471.
102 A. Shirpay and M. M. B. Mohagheghi, *Phys. B*, 2020, **587**, 412141.
103 T. Kim, H. Park, D. Joung, D. Kim, R. Lee, C. H. Shin, M. Diware, W. Chegal, S. H. Jeong, J. C. Shin, J. Park and S.-W. Kang, *Adv. Mater. Interfaces*, 2018, **5**, 1800439.
104 N. R. Pradhan, D. Rhodes, S. Feng, Y. Xin, S. Memaran, B.-H. Moon, H. Terrones, M. Terrones and L. Balicas, *ACS Nano*, 2014, **8**, 5911–5920.
105 L. Yang, W. Zhang, J. Li, S. Cheng, Z. Xie and H. Chang, *ACS Nano*, 2017, **11**, 1964–1972.
106 T. A. Empante, Y. Zhou, V. Klee, A. E. Nguyen, I. H. Lu, M. D. Valentin, S. A. Naghibi Alvillar, E. Preciado, A. J. Berges, C. S. Merida, M. Gomez, S. Bobek, M. Isarraraz, E. J. Reed and L. Bartels, *ACS Nano*, 2017, **11**, 900–905.
107 N. Qureshi, R. Patil, M. Shinde, G. Umarji, V. Causin, W. Gade, U. Mulik, A. Bhalerao and D. P. Amalnerkar, *Appl. Nanosci.*, 2015, **5**, 331–341.
108 R. Harpeness, A. Gedanken, A. M. Weiss and M. A. Slifkin, *J. Mater. Chem.*, 2003, **13**, 2603.
109 I. Uzcanga, I. Bezverkhyy, P. Afanasiev, C. Scott and M. Vrinat, *Chem. Mater.*, 2005, **17**, 3575–3577.
110 S. Xu, D. Li and P. Wu, *Adv. Funct. Mater.*, 2015, **25**, 1127–1136.
111 M. Kristl and M. Drofenik, *Inorg. Chem. Commun.*, 2003, **6**, 68–70.
112 L. Yuwen, J. Zhou, Y. Zhang, Q. Zhang, J. Shan, Z. Luo, L. Weng, Z. Teng and L. Wang, *Nanoscale*, 2016, **8**, 2720–2726.
113 F. Qi and R. Liu, *Nanoscale Res. Lett.*, 2019, **14**, 67.
114 L. Qiu, V. G. Pol, Y. Wei and A. Gedanken, *J. Mater. Chem.*, 2003, **13**, 2985.
115 B. Radisavljevic, A. Radenovic, J. Brivio, V. Giacometti and A. Kis, *Nat. Nanotechnol.*, 2011, **6**, 147–150.
116 H. Li, J. Wu, Z. Yin and H. Zhang, *Acc. Chem. Res.*, 2014, **47**, 1067–1075.
117 A. Splendiani, L. Sun, Y. Zhang, T. Li, J. Kim, C. Y. Chim, G. Galli and F. Wang, *Nano Lett.*, 2010, **10**, 1271–1275.
118 K. DiCamillo, S. Krylyuk, W. Shi, A. Davydov and M. Paranjape, *IEEE Trans. Nanotechnol.*, 2019, **18**, 144–148.
119 M. Boukhicha, M. Calandra, M.-A. Measson, O. Lancry and A. Shukla, *Phys. Rev. B: Condens. Matter Mater. Phys.*, 2013, **87**, 195316.
120 S. Tongay, J. Suh, C. Ataca, W. Fan, A. Luce, J. S. Kang, J. Liu, C. Ko, R. Raghunathanan, J. Zhou, F. Ogletree, J. Li, J. C. Grossman and J. Wu, *Sci. Rep.*, 2013, **3**, 2657.
121 Y. Hang, Q. Li, W. Luo, Y. He, X. Zhang and G. Peng, *NANO*, 2016, **11**, 1650082.
122 S. Larentis, B. Fallahazad and E. Tutuc, *Appl. Phys. Lett.*, 2012, **101**, 223104.
123 Z. Feng, Y. Xie, J. Chen, Y. Yu, S. Zheng, R. Zhang, Q. Li, X. Chen, C. Sun, H. Zhang, W. Pang, J. Liu and D. Zhang, *2D Mater.*, 2017, **4**, 025018.
124 L. Yin, X. Zhan, K. Xu, F. Wang, Z. Wang, Y. Huang, Q. Wang, C. Jiang and J. He, *Appl. Phys. Lett.*, 2016, **108**, 043503.
125 H. Nan, J. Jiang, S. Xiao, Z. Chen, Z. Luo, L. Zhang, X. Zhang, H. Qi, X. Gu, X. Wang and Z. Ni, *Nanotechnology*, 2019, **30**, 034004.
126 Y. Ke, D. Qi, C. Han, J. Liu, J. Zhu, Y. Xiang and W. Zhang, *ACS Appl. Electron. Mater.*, 2020, **2**, 920–926.
127 D. Qi, C. Han, X. Rong, X. W. Zhang, M. Chhowalla, A. T. S. Wee and W. Zhang, *ACS Nano*, 2019, **13**, 9464–9472.
128 S. Pan, W. Kong, J. Liu, X. Ge, P. Zereshki, S. Hao, D. He, Y. Wang and H. Zhao, *ACS Appl. Nano Mater.*, 2018, **2**, 459–464.
129 J. Chen, Z. Feng, S. Fan, S. Shi, Y. Yue, W. Shen, Y. Xie, E. Wu, C. Sun, J. Liu, H. Zhang, W. Pang, D. Sun, W. Feng, Y. Feng, S. Wu and D. Zhang, *ACS Appl. Mater. Interfaces*, 2017, **9**, 30107–30114.
130 A. Arora, R. Schmidt, R. Schneider, M. R. Molas, I. Breslavetz, M. Potemski and R. Bratschitsch, *Nano Lett.*, 2016, **16**, 3624–3629.
131 Y. F. Lin, Y. Xu, C. Y. Lin, Y. W. Suen, M. Yamamoto, S. Nakaharai, K. Ueno and K. Tsukagoshi, *Adv. Mater.*, 2015, **27**, 6612–6619.
132 S. Fathipour, N. Ma, W. S. Hwang, V. Protasenko, S. Vishwanath, H. G. Xing, H. Xu, D. Jena, J. Appenzeller and A. Seabaugh, *Appl. Phys. Lett.*, 2014, **105**, 192101.
133 Y. Huang, Y. H. Pan and R. Yang, *et al.*, *Nat. Commun.*, 2020, **11**, 2453.
134 M. Yang, X. Cheng, Y. Li, Y. Ren, M. Liu and Z. Qi, *Appl. Phys. Lett.*, 2017, **110**, 093108.
135 X. Li and H. Zhu, *J. Materiomics*, 2015, **1**, 33–44.
136 F. Xing, T. Li, J. Li, H. Zhu, N. Wang and X. Cao, *Nano Energy*, 2017, **31**, 590–595.
137 B.-Z. Lin, C. Ding, B.-H. Xu, Z.-J. Chen and Y.-L. Chen, *Mater. Res. Bull.*, 2009, **44**, 719–723.
138 Q. Han, S. Cai, L. Yang, X. Wang, C. Qi, R. Yang and C. Wang, *ACS Appl. Mater. Interfaces*, 2017, **9**, 21116–21123.

139 X. Wu, X. Tian, T. Chen, A. Zeng and G. Yang, *Nanotechnology*, 2018, **29**, 295604.
140 P. Byrley, M. Liu and R. Yan, *Front. Chem.*, 2019, **7**, 442.
141 S. Jiménez Sandoval, D. Yang, R. F. Frindt and J. C. Irwin, *Phys. Rev. B: Condens. Matter Mater. Phys.*, 1991, **44**, 3955–3962.
142 C. Lee, H. Yan, L. Brus, T. Heinz, J. Hone, S. Ryu, A. Splendiani, L. Sun, Y. B. Zhang, T. S. Li, J. Kim, C. Y. Chim, G. Galli and F. Wang, *Nano Lett.*, 2010, **10**, 1271.
143 J. Zhu, H. Wang, J. Liu, L. Ouyang and M. Zhu, *Nanotechnology*, 2017, **28**, 115604.
144 D. Van Thanh, C.-C. Pan, C.-W. Chu and K.-H. Wei, *RSC Adv.*, 2014, **4**, 15586–15589.
145 L. Yang, X. Cui, J. Zhang, K. Wang, M. Shen, S. Zeng, S. A. Dayeh, L. Feng and B. Xiang, *Sci. Rep.*, 2014, **4**, 1–7.
146 R. Fan, X. Chen and Z. Chen, *Chem. Lett.*, 2000, 920–921.
147 A. Midya, A. Ghorai, S. Mukherjee, R. Maiti and S. K. Ray, *J. Mater. Chem. A*, 2016, **4**, 4534–4543.
148 L. Fan, C. Zhang, G. Liang, W. Yan, Y. Guo, Y. Bi and C. Dong, *Sens. Actuators, B*, 2021, **334**, 129652.
149 X. Zhou, B. Xu, Z. Lin, D. Shu and L. Ma, *J. Nanosci. Nanotechnol.*, 2014, **14**, 7250–7254.
150 K. Krishnamoorthy, G. K. Veerasubramani, S. Radhakrishnan and S. J. Kim, *Mater. Res. Bull.*, 2014, **50**, 499–502.
151 J. Wu, Y. Liu, Y. Yao, Y. Shao and X. Wu, *J. Alloys Compd.*, 2021, **877**, 160317.
152 A. Ghorai, S. K. Ray and A. Midya, *ACS Appl. Nano Mater.*, 2021, **4**, 2999–3006.
153 K. Vasu, O. E. Meiron, A. N. Enyashin, R. Bar-Ziv and M. Bar-Sadan, *J. Phys. Chem. C*, 2018, **123**, 1987–1994.
154 R. Harpeness, A. Gedanken, A. M. Weiss and M. A. Slifkin, *J. Mater. Chem.*, 2003, **13**(10), 2603–2606.
155 S. V. P. Vattikuti, K. C. Devarayapalli, P. C. Nagajyothi and J. Shim, *Microchem. J.*, 2020, **153**, 104446.
156 W. Wen, W. Zhang, X. Wang, Q. Feng, Z. Liu and T. Yu, *Small*, 2021, **17**(36), 2102461.
157 T. Dai, Y. Liu, X. Liu, D. Xie and Y. Li, *J. Alloys Compd.*, 2019, **785**, 951–957.
158 X. Yin, Y. Li, H. Meng and W. Wu, *Appl. Surf. Sci.*, 2019, **486**, 362–370.
159 D. Kwon, J. Y. Kim, S. H. Lee, E. Lee, J. Kim, A. K. Harit, H. Y. Woo and J. Joo, *ACS Appl. Mater. Interfaces*, 2021, **13**, 40880–40890.
160 C. H. Naylor, W. M. Parkin, J. Ping, Z. Gao, Y. R. Zhou, Y. Kim, F. Streller, R. W. Carpick, A. M. Rappe, M. Drndic, J. M. Kikkawa and A. T. Johnson, *Nano Lett.*, 2016, **16**, 4297–4304.
161 J. Coleman, M. Lotya, A. Gallagher, S. Bergin, P. King, U. Khan, K. Young, A. Gaucher, S. De, R. Smith, I. Shvets, S. Arora, G. Stanton, H.-Y. Kim, K. Lee, G. Kim, G. Duesberg, T. Hallam, J. Boland and V. Nicolosi, *Science*, 2011, **331**, 568–571.
162 J. H. Huang, H. H. Hsu, D. Wang, W. T. Lin, C. C. Cheng, Y. J. Lee and T. H. Hou, *Sci. Rep.*, 2019, **9**, 8810.
163 M. Kan, H. G. Nam, Y. H. Lee and Q. Sun, *Phys. Chem. Chem. Phys.*, 2015, **17**, 14866–14871.
164 J. C. Park, S. J. Yun, H. Kim, J.-H. Park, S. H. Chae, S.-J. An, J.-G. Kim, S. M. Kim, K. K. Kim and Y. H. Lee, *ACS Nano*, 2015, **9**, 6548–6554.
165 H. W. Wang, P. Skeldon and G. E. Thompson, *Surf. Coat. Technol.*, 1997, **91**, 200–207.
166 X. Li and K. Peng, *Minerals*, 2018, **8**, 268.
167 J. Xu, J. Zhang, W. Zhang and C. S. Lee, *Adv. Energy Mater.*, 2017, **7**, 1700571.
168 G. Swain, S. Sultana and K. Parida, *Nanoscale*, 2021, **13**, 9908–9944.
169 A. Eftekhari, *Appl. Mater. Today*, 2017, **8**, 1–17.
170 J. Pu, K. Kanahashi, N. T. Cuong, C.-H. Chen, L.-J. Li, S. Okada, H. Ohta and T. Takenobu, *Phys. Rev. B*, 2016, **94**, 014312.
171 A. Ramadoss, T. Kim, G.-S. Kim and S. J. Kim, *New J. Chem.*, 2014, **38**, 2379–2385.
172 Y. Qiu, X. Li, M. Bai, H. Wang, D. Xue, W. Wang and J. Cheng, *Inorg. Chem. Front.*, 2017, **4**, 675–682.
173 C. Tsai, K. Chan, F. Abild-Pedersen and J. K. Norskov, *Phys. Chem. Chem. Phys.*, 2014, **16**, 13156–13164.
174 D. Kong, H. Wang, J. J. Cha, M. Pasta, K. J. Koski, J. Yao and Y. Cui, *Nano Lett.*, 2013, **13**, 1341–1347.
175 Z. He and W. Que, *Appl. Mater. Today*, 2016, **3**, 23–56.
176 J. Guo, Y. Shi, X. Bai, X. Wang and T. Ma, *J. Mater. Chem. A*, 2015, **3**, 24397–24404.
177 Q. Tang and D.-e Jiang, *ACS Catal.*, 2016, **6**, 4953–4961.
178 M. A. Lukowski, A. S. Daniel, F. Meng, A. Forticaux, L. Li and S. Jin, *J. Am. Chem. Soc.*, 2013, **135**, 10274–10277.
179 D. Voiry, M. Salehi, R. Silva, T. Fujita, M. Chen, T. Asefa, V. B. Shenoy, G. Eda and M. Chhowalla, *Nano Lett.*, 2013, **13**, 6222–6227.
180 J. Zhang, T. Wang, P. Liu, Y. Liu, J. Ma and D. Gao, *Electrochim. Acta*, 2016, **217**, 181–186.
181 Y. Huang, Y.-E. Miao, J. Fu, S. Mo, C. Wei and T. Liu, *J. Mater. Chem. A*, 2015, **3**, 16263–16271.
182 A. Singh, J. Rohilla, M. S. Hassan, T. Devaiah C, P. P. Ingole, P. K. Santra, D. Ghosh and S. Sapra, *ACS Appl. Nano Mater.*, 2022, **5**, 4293–4304.
183 J. C. McGlynn, I. Cascallana-Matías, J. P. Fraser, I. Roger, J. McAllister, H. N. Miras, M. D. Symes and A. Y. Ganin, *Energy Technol.*, 2018, **6**, 345–350.
184 J. Seok, J.-H. Lee, S. Cho, B. Ji, H. W. Kim, M. Kwon, D. Kim, Y.-M. Kim, S. H. Oh and S. W. Kim, *2D Mater.*, 2017, **4**, 025061.
185 H. Qiao, Z. Huang, S. Liu, Y. Liu, J. Li and X. Qi, *Ceram. Int.*, 2018, **44**, 21205–21209.
186 D. Lu, X. Ren, L. Ren, W. Xue, S. Liu, Y. Liu, Q. Chen, X. Qi and J. Zhong, *ACS Appl. Energy Mater.*, 2019, **3**, 3212–3219.
187 A. Midya, A. Ghorai, S. Mukherjee, R. Maiti and S. K. Ray, *J. Mater. Chem. A*, 2016, **4**, 4534–4543.
188 M.-h Wu, L. Li, N. Liu, D.-j Wang, Y.-c Xue and L. Tang, *Process Saf. Environ. Prot.*, 2018, **118**, 40–58.
189 Y. Wu, M. Xu, X. Chen, S. Yang, H. Wu, J. Pan and X. Xiong, *Nanoscale*, 2016, **8**, 440–450.
190 H. Mittal and M. Khanuja, *Dyes Pigm.*, 2020, **175**, 108109.
191 J. Huang, B. Jin, H. Liu, X. Li, Q. Zhang, S. Chu, R. Peng and S. Chu, *J. Mater. Chem. A*, 2018, **6**, 11424–11434.

192 H. Huang, J. Wang, W. Hu, L. Liao, P. Wang, X. Wang, F. Gong, Y. Chen, G. Wu and W. Luo, *Nanotechnology*, 2016, **27**, 445201.
193 Z. Wang and B. Mi, *Environ. Sci. Technol.*, 2017, **51**, 8229–8244.
194 E. Fosso-Kankeu, N. Kumar, S. Pandey and S. S. Ray, IMWA 2019 "Mine Water: Technological and Ecological Challenges", 2019, pp. 175–178.
195 K. Ai, C. Ruan, M. Shen and L. Lu, *Adv. Funct. Mater.*, 2016, **26**, 5542–5549.
196 X. Wang, J. Ding, S. Yao, X. Wu, Q. Feng, Z. Wang and B. Geng, *J. Mater. Chem. A*, 2014, **2**, 15958–15963.
197 A. T. Massey, R. Gusain, S. Kumari and O. P. Khatri, *Ind. Eng. Chem. Res.*, 2016, **55**, 7124–7131.
198 H. Song, S. You and X. Jia, *Appl. Phys. A: Mater. Sci. Process.*, 2015, **121**, 541–548.
199 P. K. Chow, E. Singh, B. C. Viana, J. Gao, J. Luo, J. Li, Z. Lin, A. L. Elías, Y. Shi, Z. Wang, M. Terrones and N. Koratkar, *ACS Nano*, 2015, **9**, 3023–3031.
200 C. Liu, Q. Wang, F. Jia and S. Song, *J. Mol. Liq.*, 2019, **292**, 111390.
201 M. Heiranian, A. B. Farimani and N. R. Aluru, *Nat. Commun.*, 2015, **6**, 8616.
202 E. Singh, P. Singh, K. S. Kim, G. Y. Yeom and H. S. Nalwa, *ACS Appl. Mater. Interfaces*, 2019, **11**, 11061–11105.
203 Y. Yoon, K. Ganapathi and S. Salahuddin, *Nano Lett.*, 2011, **11**, 3768–3773.
204 K. I. Bolotin, K. J. Sikes, Z. Jiang, M. Klima, G. Fudenberg, J. Hone, P. Kim and H. L. Stormer, *Solid State Commun.*, 2008, **146**, 351–355.
205 D. Sarkar, X. Xie, J. Kang, H. Zhang, W. Liu, J. Navarrete, M. Moskovits and K. Banerjee, *Nano Lett.*, 2015, **15**, 2852–2862.
206 H. Li, Z. Yin, Q. He, H. Li, X. Huang, G. Lu, D. W. Fam, A. I. Tok, Q. Zhang and H. Zhang, *Small*, 2012, **8**, 63–67.
207 H. Li, J. Wu, Z. Yin and H. Zhang, *Acc. Chem. Res.*, 2014, **47**, 1067–1075.
208 H. Li, Z. Yin, Q. He, H. Li, X. Huang, G. Lu, D. W. H. Fam, A. I. Y. Tok, Q. Zhang and H. Zhang, *Small*, 2012, **8**, 63–67.
209 S. Guo, D. Yang, S. Zhang, Q. Dong, B. Li, N. Tran, Z. Li, Y. Xiong and M. E. Zaghloul, *Adv. Funct. Mater.*, 2019, **29**, 1900138.
210 M. Donarelli, S. Prezioso, F. Perrozzi, F. Bisti, M. Nardone, L. Giancaterini, C. Cantalini and L. Ottaviano, *Sens. Actuators, B*, 2015, **207**, 602–613.
211 S. Yang, C. Jiang and S.-h Wei, *Appl. Phys. Rev.*, 2017, **4**, 021304.
212 S. Singh, S. Sharma, R. C. Singh and S. Sharma, *Appl. Surf. Sci.*, 2020, **532**, 147373.
213 C. Fan, Z. Wei, S. Yang and J. Li, *RSC Adv.*, 2014, **4**, 775–778.
214 H. S. Lee, S. W. Min, Y. G. Chang, M. K. Park, T. Nam, H. Kim, J. H. Kim, S. Ryu and S. Im, *Nano Lett.*, 2012, **12**, 3695–3700.
215 O. Lopez-Sanchez, D. Lembke, M. Kayci, A. Radenovic and A. Kis, *Nat. Nanotechnol.*, 2013, **8**, 497–501.
216 V. Selamneni, N. Nerurkar and P. Sahatiya, *IEEE Sens. Lett.*, 2020, **4**, 1–4.
217 S. Larentis, B. Fallahazad, H. C. P. Movva, K. Kim, A. Rai, T. Taniguchi, K. Watanabe, S. K. Banerjee and E. Tutuc, *ACS Nano*, 2017, **11**, 4832–4839.
218 A. Giri, H. Yang, W. Jang, J. Kwak, K. Thiyagarajan, M. Pal, D. Lee, R. Singh, C. Kim, K. Cho, A. Soon and U. Jeong, *Chem. Mater.*, 2018, **30**, 2463–2473.
219 Q. He, Z. Zeng, Z. Yin, H. Li, S. Wu, X. Huang and H. Zhang, *Small*, 2012, **8**, 2994–2999.
220 Y. Yang, T. Liu, L. Cheng, G. Song, Z. Liu and M. Chen, *ACS Appl. Mater. Interfaces*, 2015, **7**, 7526–7533.
221 C. Zhu, Z. Zeng, H. Li, F. Li, C. Fan and H. Zhang, *J. Am. Chem. Soc.*, 2013, **135**, 5998–6001.
222 R. Kurapati, L. Muzi, A. P. R. de Garibay, J. Russier, D. Voiry, I. A. Vacchi, M. Chhowalla and A. Bianco, *Adv. Funct. Mater.*, 2017, **27**, 1605176.
223 H. Deng, X. Yang and Z. Gao, *Analyst*, 2015, **140**, 3210–3215.
224 D. Sarkar, W. Liu, X. Xie, A. C. Anselmo, S. Mitragotri and K. Banerjee, *ACS Nano*, 2014, **8**, 3992–4003.
225 T. Lin, L. Zhong, L. Guo, F. Fu and G. Chen, *Nanoscale*, 2014, **6**, 11856–11862.
226 A. K. Mishra, S. K. Mishra and R. K. Verma, *J. Phys. Chem. C*, 2016, **120**, 2893–2900.
227 T. Nawz, A. Safdar, M. Hussain, D. Sung Lee and M. Siyar, *Crystals*, 2020, **10**, 902.
228 S. Hussain, S. F. Shaikh, D. Vikraman, R. S. Mane, O.-S. Joo, M. Naushad and J. Jung, *Chem. Phys. Chem.*, 2015, **16**, 3959–3965.
229 Y. Yang, N. Huo and J. Li, *J. Mater. Chem. C*, 2017, **5**, 7051–7056.
230 E. Bi, H. Chen, X. Yang, F. Ye, M. Yin and L. Han, *Sci. Rep.*, 2015, **5**, 13214.
231 S. Hussain, S. A. Patil, D. Vikraman, I. Rabani, A. A. Arbab, S. H. Jeong, H.-S. Kim, H. Choi and J. Jung, *Appl. Surf. Sci.*, 2020, **504**, 144401.
232 M. Bernardi, M. Palummo and J. C. Grossman, *Nano Lett.*, 2013, **13**, 3664–3670.
233 H. Lian, M. Pan, J. Han, X. Cheng, J. Liang, W. Hua, Y. Qu, Y. Wu, Q. Dong, B. Wei, H. Yan and W.-Y. Wong, *J. Mater. Chem. A*, 2021, **9**, 16500–16509.
234 K. J. Hsiao, J. D. Liu, H. H. Hsieh and T. S. Jiang, *Phys. Chem. Chem. Phys.*, 2013, **15**, 18174–18178.
235 H.-y Sun, P.-h Li, Y.-m Xue, Z.-x Qiao and L. Sai, *Optoelectron. Lett.*, 2019, **15**, 428–434.
236 J. Hao, G. Song, T. Liu, X. Yi, K. Yang, L. Cheng and Z. Liu, *Adv. Sci.*, 2017, **4**, 1600160.
237 Z. Wang, A. von dem Bussche, Y. Qiu, T. M. Valentin, K. Gion, A. B. Kane and R. H. Hurt, *Environ. Sci. Technol.*, 2016, **50**, 7208–7217.